



Dobra, T. E., Lawrie, A. G. W., & Dalziel, S. B. (2022). A hierarchical decomposition of internal wave fields. *Journal of Fluid Mechanics*, 934, [A33]. <https://doi.org/10.1017/jfm.2021.1115>

Peer reviewed version

License (if available):  
CC BY-NC-ND

Link to published version (if available):  
[10.1017/jfm.2021.1115](https://doi.org/10.1017/jfm.2021.1115)

[Link to publication record in Explore Bristol Research](#)  
PDF-document

This is the author accepted manuscript (AAM). The final published version (version of record) is available online via Cambridge University Press at <https://doi.org/10.1017/jfm.2021.1115> . Please refer to any applicable terms of use of the publisher.

## University of Bristol - Explore Bristol Research

### General rights

This document is made available in accordance with publisher policies. Please cite only the published version using the reference above. Full terms of use are available: <http://www.bristol.ac.uk/red/research-policy/pure/user-guides/ebr-terms/>

Banner appropriate to article type will appear here in typeset article

# A hierarchical decomposition of internal wave fields

Thomas E. Dobra<sup>1,2</sup>, Andrew G. W. Lawrie<sup>1</sup>† and Stuart B. Dalziel<sup>2</sup>

<sup>1</sup>Hele-Shaw Laboratory, University of Bristol, University Walk, Bristol, BS8 1TR, UK

<sup>2</sup>Department of Applied Mathematics and Theoretical Physics, University of Cambridge, Wilberforce Road, Cambridge, CB3 0WA, UK

(Received xx; revised xx; accepted xx)

Internal gravity wave fields are decomposed into temporal modes revealing the hierarchical structure of nonlinear wave–wave interactions. We present a novel fusion of Green’s functions for solving the forced internal wave equation with a weakly nonlinear perturbation expansion. Our approach is semi-analytical, based on integration over finite elements with the perturbation expansion ensuring source terms at each order are only dependent on the solutions at lower orders. Thus, the procedure is purely inductive and efficient to compute. To perform a thorough validation of our new method, we diagnose experiments using Synthetic Schlieren and apply sophisticated post-processing techniques, including Dynamic Mode Decomposition, to obtain these temporal modes for systems with discrete input frequencies. By decomposing the experimental field and comparing individual constituents against equivalents synthesised by our model, we are able to present the first truly comprehensive, validated, mechanistic picture of wave–wave interactions to arbitrary order. This synergy enables us to identify non-wave oscillatory behaviour at frequencies shared by waves in the hierarchy and leads us to discover an important open question regarding transmission efficiency within individual wave–wave interactions. Although our experiments are generated by boundary displacements, we present equivalences between source terms and boundary displacements so that the class of applicable systems may be broadened. Our technique also generalises to aperiodic and unbounded configurations and to any weakly nonlinear wave-governed system for which there is an available Green’s function.

**Key words:** Internal waves, Ocean processes, Stratified flows, Topographic effects, Computational methods, Wave scattering, Solitary waves

## 1. Introduction

The interior of the oceans may be considered as a vast field of internal gravity waves. Continuous stratification, gravitational forcing due to the lunar orbit (Rattray 1960) and suitable bathymetry conspire to produce a complex interior system of mechanical wave transmission. Amplitudes of these waves may be hundreds of metres (Susanto *et al.* 2005), but they are known to propagate at shallow angles and in beam-like geometric patterns. In

† Email address for correspondence: andrew.lawrie@bristol.ac.uk

34 general, waveforms are modified by boundary topography (van Haren *et al.* 2002), and in  
35 particular, their spectral form is crucial to predicting their interaction. There are several well  
36 known features of internal wave mechanics that arise due to nonlinearity in the underlying  
37 physics, and primarily these arise from the quadratic structure of the advection operator.  
38 Viewed in spectral space, the advection operator may be cast as a geometric relationship  
39 between wavevectors and frequencies known as triadic interaction (Phillips 1960; Thorpe  
40 1966). Special cases include the interaction of two crossing wave beams (McComas &  
41 Bretherton 1977; Sun & Kunze 1999 $a,b$ ; Javam *et al.* 2000; Tabaei *et al.* 2005; Smith &  
42 Crockett 2014), triadic resonant instability (Davis & Acrivos 1967; Martin *et al.* 1969;  
43 McEwan 1971; Bourget *et al.* 2013) and a limiting case known as parametric subharmonic  
44 instability (McEwan & Robinson 1975; Benielli & Sommeria 1998; Koudella & Staquet  
45 2006; Karimi & Akylas 2014). We will discuss in depth interactions of crossing wave beams  
46 as part of this paper, but we refer the reader to Dauxois *et al.* (2018) for a review of instabilities  
47 and Müller *et al.* (1986) for a broader overview.

48 Experiments have played an important role in refining our understanding of internal  
49 wave systems ranging from early studies of oscillating cylinders (Görtler 1943; Mowbray  
50 & Rarity 1967) to complex mechanical devices for generating quasi-planar waves (McEwan  
51 1971; Gostiaux *et al.* 2007). There are broadly three approaches to analysing wave systems:  
52 characteristics, Green’s functions and Fourier methods. The oscillating cylinder is the natural  
53 analogue of characteristic (Hurley 1972) and Green’s function approaches (Hurley 1969;  
54 Voisin 1991), because spatially localised beams emerge in a St. Andrew’s cross pattern and  
55 these are aligned with the characteristics. On the other hand, Fourier methods more naturally  
56 correspond to quasi-planar systems (Mercier *et al.* 2010), where there is implicit spatial  
57 periodicity as well as temporal periodicity.

58 In this paper, we shall build a more general framework based on Green’s functions and seek  
59 to validate using laboratory experiments, firstly on a polychromatic aperiodic example case  
60 of lee waves, and then develop to a case where steady, periodic wave beams show significant  
61 nonlinear interaction. The experiments utilise the unique capabilities of the “magic carpet”  
62 (Dobra *et al.* 2019) to generate a full spectrum of wave beams, Synthetic Schlieren (Dalziel  
63 *et al.* 1998; Sutherland *et al.* 1999; Dalziel *et al.* 2000; ?) to diagnose the resulting wave  
64 field from density gradients, and Dynamic Mode Decomposition (Schmid 2010) to dissect  
65 the modal structure. Using these tools, figure 1 illustrates a typical wave–wave interaction  
66 with two incident beams in subfigures 1( $a$ ) and 1( $b$ ) with direction of propagation shown  
67 by the arrows. Subfigure 1( $c$ ) shows a snapshot of the experimentally observed field, and  
68 subfigures 1( $d$ )–( $f$ ) show “daughter” modes that are observed to emerge nonlinearly from  
69 the interaction and have directions of propagation as shown.

70 To address the question of nonlinear wave–wave interactions, our new framework will  
71 allow for weakly nonlinear interactions between a hierarchy of Green’s functions. We utilise  
72 Green’s functions to represent the driving waves and derive the weakly nonlinear transfer  
73 terms that pass energy into other frequency and wavenumber components, these also being  
74 represented in terms of Green’s functions. Our framework is sufficiently broad to deal not  
75 only with interactions of the form shown in figure 1 that lead to resonance (disturbances  
76 that satisfy both the geometric conditions on wavenumber and frequency and also satisfy  
77 the relevant dispersion relation) but also those where the linear dispersion relation is not  
78 satisfied.

79 The structure of this article is as follows. We present the background material to the  
80 governing equations in §2 and discuss the tractability of other analytical options. Focussing  
81 on the monochromatic Green’s function solution to the linear equation in §3, we prepare the  
82 building blocks of a hierarchical numerical approach. In §4, we demonstrate application of  
83 this approach to inviscid, aperiodic systems, and carefully validate against experiments using

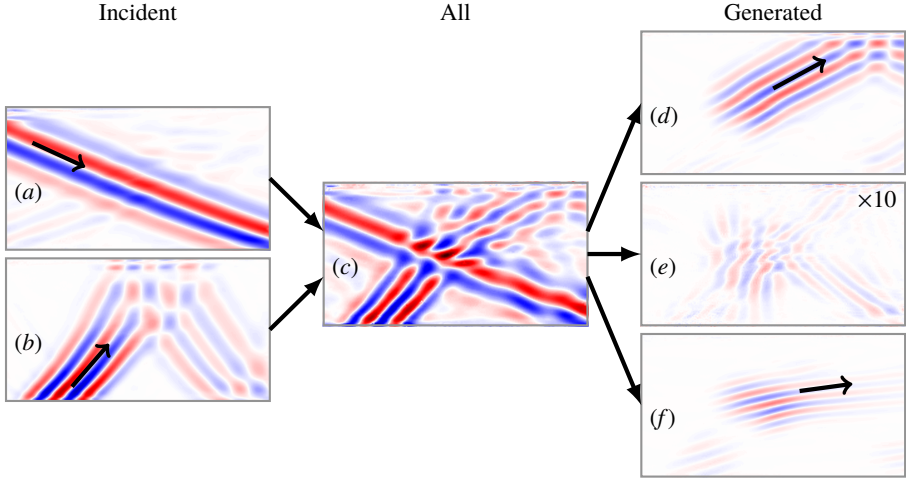


Figure 1: Schematic showing a decomposition of a wave–wave interaction between two incident internal wave beams ((a) and (b)). Subfigure (c) shows the full experimentally observed wave field. Subfigures (d)–(f) show nonlinearly generated “daughter” modes that are identifiable from the experiment. The arrows indicate the direction of propagation of each wave beam.

84 our “magic carpet” (Dobra *et al.* 2019). We then generalise in §5 our numerical Green’s  
 85 function approach so that we may capture the physics of nonlinearly interacting internal  
 86 waves. We employ the perturbation expansion technique of Tabaei *et al.* (2005) and developed  
 87 further in Dobra *et al.* (2021) to account for successive layers of wave–wave interactions and  
 88 demonstrate that the resultant field compares well with experimental observations. Finally,  
 89 in §6, we draw our conclusions.

## 90 2. Internal wave equation

91 We begin by considering two-dimensional, inviscid, linear internal waves in a quiescent,  
 92 Boussinesq density stratification,  $\rho_0(z)$ . These restrictions closely approximate the conditions  
 93 in our laboratory experiments, where it is particularly advantageous to consider flows with  
 94 limited variation in the third dimension for ease of diagnosis. We define  $\mathbf{x} = (x, z)$  as  
 95 the horizontal and vertical coordinates with corresponding unit basis vectors  $\{\mathbf{e}_x, \mathbf{e}_z\}$ , and  
 96 we assume there is no diffusion of mass or heat. Let  $t$  be time,  $\mathbf{u} = (u, w)$  the velocity  
 97 field,  $p'$  the perturbation from hydrostatic pressure,  $\rho_{00}$  be the Boussinesq reference density,  
 98  $\rho'$  (with  $|\rho'| \ll \rho_{00}$ ) the perturbation from  $\rho_0(z)$  and  $g$  gravitational acceleration. Then, the  
 99 three nonlinear governing equations are the conservation of momentum (Euler equation),

$$100 \quad \rho_{00} \left( \frac{\partial \mathbf{u}}{\partial t} + \mathbf{u} \cdot \nabla \mathbf{u} \right) = -\nabla p' - \rho' g \mathbf{e}_z, \quad (2.1)$$

101 the conservation of volume (equivalent to incompressibility in the case of a homogeneous  
 102 fluid),

$$103 \quad \nabla \cdot \mathbf{u} = 0, \quad (2.2)$$

104 and consequently the conservation of mass may be written as

$$105 \quad \frac{\partial \rho'}{\partial t} + \mathbf{u} \cdot \nabla (\rho_0 + \rho') = 0. \quad (2.3)$$

106 In the linear wave approximation, the two nonlinear terms arising from the advection operator  
 107  $\mathbf{u} \cdot \nabla$  are considered to be negligible. The remaining derivative operators can be isolated  
 108 into a complex matrix  $\mathbf{P}$  that acts on a state vector  $\phi$ , say, and the system arranged into  
 109 homogeneous form. Taking a single Fourier mode of  $\phi$  with wavevector  $\mathbf{k} = (k, m)$  and  
 110 frequency  $\omega$ , we can write

$$111 \quad \phi = \hat{\phi} e^{i(\mathbf{k} \cdot \mathbf{x} - \omega t)}. \quad (2.4)$$

112 The derivative operator,  $\mathbf{P}$ , then takes the complex algebraic form  $\hat{\mathbf{P}}$ . For a homogeneous  
 113 system, non-trivial symmetries are found when the determinant  $|\hat{\mathbf{P}}| = 0$ , and these correspond  
 114 to resonant wave behaviours. From

$$115 \quad |\hat{\mathbf{P}}| = \omega^2 - \left( -\frac{g}{\rho_{00}} \frac{d\rho_0}{dz} \right) \frac{k^2}{|\mathbf{k}|^2} = 0 \quad (2.5)$$

116 arises a natural frequency, the buoyancy (Brunt–Väisälä) frequency,

$$117 \quad N = \sqrt{-\frac{g}{\rho_{00}} \frac{d\rho_0}{dz}}, \quad (2.6)$$

118 and by examining the geometry of  $k/|\mathbf{k}|$ , the dispersion relation,

$$119 \quad \omega = N \cos \Theta, \quad (2.7)$$

120 is obtained, where  $\Theta$  is the angle between wavevector  $\mathbf{k}$  and the horizontal. Since this system  
 121 is linear, any perturbation quantity  $\chi$  satisfies the dispersion relation provided that

$$122 \quad (\omega^2 |\mathbf{k}|^2 - N^2 k^2) \hat{\chi} = 0. \quad (2.8)$$

123 Taking the inverse Fourier transform yields the linear internal wave equation,

$$124 \quad \left( \frac{\partial^2}{\partial t^2} \nabla^2 + N^2 \frac{\partial^2}{\partial x^2} \right) \chi = \mathcal{L} \chi = 0, \quad (2.9)$$

125 where we define  $\mathcal{L}$  to be the corresponding operator. From any choice of  $\chi$ , the polarisation  
 126 of any other quantity can be derived by appropriate substitution into the linearised equations.  
 127 In particular, any such quantity will also satisfy the linear internal wave equation.

128 Source terms may be configured to be equivalent to the action of boundaries, and we will  
 129 see in §5 that they can also inductively account for discrepancies between a linear wave  
 130 approximation and the corresponding nonlinear field. Thus, we consider solution approaches  
 131 to the inhomogeneous internal wave equation,  $\mathcal{L} \chi = f$ , with source distribution  $f(\mathbf{x}, t)$ .

132 While we could choose to work with any variable  $\chi$ , it is important to select a representation  
 133 of the system that has a clear physical interpretation. In view of this, two interesting choices  
 134 of  $\chi$  are an internal potential,  $\xi$ , as used by Voisin (1994) and Scase & Dalziel (2004), and  
 135 the streamfunction,  $\psi$ . We now consider the physical interpretation of point source terms for  
 136 each of these potentials in turn.

137 The internal potential is defined by

$$138 \quad \mathbf{u} = \left( \frac{\partial^2}{\partial t^2} \nabla + N^2 \mathbf{e}_x \frac{\partial}{\partial x} \right) \xi = \left( \left( \frac{\partial^2}{\partial t^2} + N^2 \right) \frac{\partial \xi}{\partial x}, \frac{\partial^3 \xi}{\partial t^2 \partial z} \right), \quad (2.10)$$

139 and is chosen such that  $\nabla \cdot \mathbf{u} = \mathcal{L} \xi$ . We consider an instantaneous point source of unit  
 140 strength at  $\mathbf{x}_0$  that is active at time  $t_0$ , expressed in terms of Dirac- $\delta$  functions as  $f =$   
 141  $\delta(\mathbf{x} - \mathbf{x}_0) \delta(t - t_0)$ . Integrating along a short time interval including  $t_0$  over some fixed

142 volume  $V$  around  $\mathbf{x}_0$  with boundary  $\partial V$  and using the divergence theorem gives

$$143 \quad \int_{t_0-\epsilon}^{t_0+\epsilon} \int_V f \, dV \, dt = \int_{t_0-\epsilon}^{t_0+\epsilon} \int_V \mathcal{L}\xi \, dV \, dt = \int_{t_0-\epsilon}^{t_0+\epsilon} \int_{\partial V} \mathbf{u} \cdot d\mathbf{S} \, dt, \quad (2.11)$$

144 which is the total volume of fluid ejected through enclosing surface,  $S$ . Therefore, the point  
145 source injects one unit of fluid volume.

146 The streamfunction,  $\psi$ , is an integral of the velocity field according to

$$147 \quad \mathbf{u} = \nabla \times (\psi \mathbf{e}_y) = \left( -\frac{\partial \psi}{\partial z}, \frac{\partial \psi}{\partial x} \right). \quad (2.12)$$

148 It follows immediately that the vorticity  $\nabla \times \mathbf{u} = -\nabla^2 \psi$ , and it appears in the first term of the  
149 internal wave equation (2.9) if we set  $\chi = \psi$ . Expressing the linear terms of (2.3) in terms  
150 of  $\psi$ , multiplying by  $g/\rho_{00}$  and differentiating with respect to  $x$ , we obtain

$$151 \quad N^2 \frac{\partial^2 \psi}{\partial x^2} = \frac{g}{\rho_{00}} \frac{\partial^2 \rho'}{\partial x \partial t}. \quad (2.13)$$

152 The left-hand side appears in (2.9) and so we may integrate with respect to  $t$  to obtain the  
153 vorticity equation,

$$154 \quad -\frac{\partial}{\partial t} \nabla^2 \psi - \frac{g}{\rho_{00}} \frac{\partial \rho'}{\partial x} = 0, \quad (2.14)$$

155 which can also be derived directly from the linearised momentum equation. Vorticity in a  
156 fixed control volume changes only due to baroclinic generation or by the introduction of  
157 sources applied on the right-hand side of (2.14). For a source  $f = \delta(\mathbf{x} - \mathbf{x}_0) \delta(t - t_0)$  in the  
158 internal wave equation (2.9), the corresponding vorticity source in (2.14) may be expressed  
159 in terms of the Heaviside step function,  $H$ , as  $\int f \, dt = \delta(\mathbf{x} - \mathbf{x}_0) H(t - t_0)$ , which we may  
160 interpret as a supply of vorticity at unit rate after  $t_0$ .

161 While steady-state waves in any system violate causality, they provide a good approx-  
162 imation to their long term behaviour, so in practice, we use monochromatic sources of the  
163 form  $f = \delta(\mathbf{x} - \mathbf{x}_0) \exp(-i\omega t)$ . For the internal potential,  $\xi$ , the volume source is of unit  
164 amplitude and is in phase with  $f$ , and for the streamfunction,  $\psi$ , the vorticity is modified by  
165 a factor of  $-i/\omega$ .

166 With any choice of  $\chi$ , one candidate approach uses Fourier transforms in both time and  
167 space (denoted by a circumflex) to yield the following algebraic equation,

$$168 \quad \hat{\psi} = \frac{\hat{f}}{\omega^2 |\mathbf{k}|^2 - N^2 k^2}, \quad (2.15)$$

169 We note however that the denominator is zero for any Fourier modes that satisfy the dispersion  
170 relation, and these correspond to resonant modes. In common with a simple harmonic  
171 oscillator, the amplitudes of resonant modes grow linearly. This growth may occur in time,  
172 however over a broad class of wave equations that exist in multiple dimensions, growth may  
173 equally occur along spatial directions, and this remains the case for any linear combination  
174 of space–time directions (Dobra 2018). Although in the internal wave system each mode  
175 is a plane wave of infinite extent, a broadband linear superposition of such modes may be  
176 configured to produce an internal wave beam in space with finite width. Counterintuitively,  
177 there exists the limiting case of steady-state resonance, where all of the energy is transported  
178 away from the source and amplitude growth is found in purely spatial directions.

179 Dobra (2018) combined these resonant waves with non-resonant forced oscillations to  
180 obtain an integral solution in terms of inverse Fourier transforms. However, exact solutions  
181 only apply to periodic domains, yet the experimental configurations we consider in §§4–5 are

182 best approximated by a combination of reflecting and non-reflecting boundary conditions,  
 183 which Fourier methods do not in general support. Given that an intermediate aim in §3  
 184 is to establish a numerical method with broad enough generality to handle aperiodicity in  
 185 both space and time, we must explore alternative techniques for a computationally efficient  
 186 implementation.

187 One such approach uses a suitably chosen Green’s function, encoding the system response  
 188 to a point source. A distribution of point sources in space and time may be configured to  
 189 represent an arbitrary excitation of the system, and in this work we consider distributions that  
 190 produce interference patterns representing both boundary displacements and mode–mode in-  
 191 teractions. For the simplest point source,  $f = \delta(\mathbf{x} - \mathbf{x}_0) \delta(t - t_0)$ , Sekerzh-Zen’kovich (1981)  
 192 derived the instantaneous Green’s function by Fourier transforming in space only, solving  
 193 the resulting ordinary differential equation in time and taking the inverse transform. Once  
 194 again, however, we have non-vanishing solutions at the boundary, and in any finite domain  
 195 (such as one requires to compute an approximate numerical solution), the Green’s function  
 196 obtained using Fourier techniques encodes the response to a periodic array of isolated point  
 197 sources. By instead using a sustained monochromatic source,  $f = \delta(\mathbf{x} - \mathbf{x}_0) \exp(-i\omega t)$ , we  
 198 will obtain a solution in terms of elementary functions (see §3), so we will avoid difficulties  
 199 with non-vanishing solutions at the boundary.

### 200 3. Monochromatic Green’s function

#### 201 3.1. Analysis

202 The monochromatic Green’s function,  $G_\omega(\mathbf{x}; \mathbf{x}_0)$ , is the solution to the internal wave equation  
 203 with point forcing as given by

$$204 \left( \frac{\partial^2}{\partial t^2} \nabla^2 + N^2 \frac{\partial^2}{\partial x^2} \right) G_\omega \exp(-i\omega t) = \delta(\mathbf{x} - \mathbf{x}_0) \exp(-i\omega t). \quad (3.1)$$

205 Provided we have a solution for  $G_\omega$ , the solution to the internal wave equation with source  
 206 distribution of the form  $f = f_\omega(x, z) \exp(-i\omega t)$  is

$$207 \chi_\omega(\mathbf{x}) = \int_{\mathbb{R}^2} G_\omega(\mathbf{x}; \mathbf{x}_0) f_\omega(\mathbf{x}_0) d^2\mathbf{x}_0, \quad (3.2)$$

208 where  $\mathbb{R}$  is the set of real numbers.

209 The precise form of the Green’s function depends on the configuration of the domain  
 210 and boundary conditions. In the well-studied case of internal tides (e.g. Robinson 1969;  
 211 Pétrélis *et al.* 2006; Balmforth & Peacock 2009), the appropriate Green’s function takes the  
 212 form of a sum of normal modes. However, this is less general than the spatially unbounded  
 213 case considered by Voisin (1991), who presented a comprehensive derivation of the three-  
 214 dimensional Green’s functions. His work considered both instantaneous and monochromatic  
 215 sources and considers in some depth the implications for causality of using Green’s functions  
 216 for internal waves. Motivated by physical arguments, earlier work by Hurley (1969) quoted  
 217 the two-dimensional streamfunction due to a monochromatic point vorticity source, which  
 218 we identify as  $-i\omega G_\omega$  in our own work, but this does not include the instantaneous source  
 219 solution we discussed at the end of §2. This is important because instantaneous sources are  
 220 potentially an attractive foundation for a semi-analytical model with sufficient generality to  
 221 study both wave and non-wave perturbations to a density field. Unfortunately, there is no  
 222 numerical method for an unbounded Fourier transform, and there are concerns over causality  
 223 in the spatially periodic domain that we would require for a corresponding numerical method.  
 224 The simplest causal foundation is the monochromatic source. We note in addition that both

225 Hurley and Voisin use exponential, rather than linear, density stratifications. The exponential  
 226 form leads to a distinct interpretation of the buoyancy frequency,  $N$ , and the linear wave  
 227 equation includes an additional term arising from the curvature of the stratification. The  
 228 solutions are related by a conformal map. Given these points and further technical intricacies  
 229 that are specific to the two-dimensional case and influenced our choice of integration scheme,  
 230 there is some justification for presenting our own solution in preparation for a flexible, general  
 231 numerical implementation.

232 Our solution approach is summarised as follows, with full details in appendix A. Evaluating  
 233 the time derivatives in (3.1), defining the constant  $\Gamma = (1 - (N/\omega)^2)^{1/2}$  and cancelling the  
 234 temporal exponential terms yields

$$\Gamma^2 \frac{\partial^2 G_\omega}{\partial x^2} + \frac{\partial^2 G_\omega}{\partial z^2} = -\frac{\delta(\mathbf{x} - \mathbf{x}_0)}{\omega^2}. \quad (3.3)$$

236 We note that  $\Gamma$  is real for evanescent internal waves,  $|\omega| > N$ , but is imaginary for  $|\omega| < N$ .  
 237 For  $\Gamma \in \mathbb{R}$ , this elliptic equation is a skewed Poisson's equation, and a dilatation allows us to  
 238 use the free space Green's function for the unskewed Poisson's equation. Let  $r$  be the distance  
 239 from the source in the transformed space so that

$$r^2 = \frac{(x - x_0)^2}{1 - \left(\frac{N}{\omega}\right)^2} + (z - z_0)^2, \quad (3.4)$$

241 then the standard Green's function for a source that will generate an evanescent wave is

$$G_\omega = -\frac{\log(r^2)}{4\pi\omega^2\Gamma}. \quad (3.5)$$

243 Analytic continuation from  $|\omega| > N$  to all  $\omega \in \mathbb{R}$  enables a solution to the corresponding  
 244 hyperbolic equation, and wavepackets propagate along the real-valued characteristics, as  
 245 discussed in Dobra *et al.* (2021). There are branch points where the argument of a logarithm  
 246 or a number raised to a fractional power is zero or infinity, so the branch points are at  
 247  $r^2 = \{0, \infty\}$  and  $1/\Gamma = \{0, \infty\}$ , which gives the branch points

$$\omega = 0, \pm \frac{N}{\sqrt{1 + \left(\frac{x-x_0}{z-z_0}\right)^2}} \text{ and } \pm N. \quad (3.6)$$

249 The  $r^2 = 0$  branch points only occur where  $|\omega| \leq N$  and are on the characteristics  
 250 passing through  $\mathbf{x}_0$ . We assemble the Green's function for each solution region in table 3  
 251 in appendix A, where we classify by the complex argument of  $r^2$  and  $1/\Gamma$ . By defining  
 252  $\gamma = ((N/\omega)^2 - 1)^{1/2} = \tan \Theta$ , as may be inferred from the dispersion relation (2.7), we  
 253 condense all the propagating cases to

$$G_\omega = i \operatorname{sgn}(\omega) \frac{\log\left|\left(\frac{x-x_0}{\gamma}\right)^2 - (z-z_0)^2\right|}{4\pi\omega^2\gamma} + \frac{1}{4\omega^2\gamma} \operatorname{H}\left(\left(\frac{x-x_0}{\gamma}\right)^2 - (z-z_0)^2\right). \quad (3.7)$$

255 For sources that generate evanescent waves, the Green's function is real, so the response  
 256 is in phase with the forcing. A contour plot of the Green's function is shown in figure 2.  
 257 As  $\omega \rightarrow \infty$ , or equivalently as  $N \rightarrow 0$ , the elliptical contours broaden to become circular.  
 258 In the limiting case, this is the unstratified potential flow response corresponding to our  
 259 choice of  $\chi$ . The contours of the streamfunction,  $\psi$ , always represent streamlines in the flow,  
 260 whereas only in the case when the internal potential,  $\xi$ , is monochromatic and  $N = 0$  do  
 261 its contours coincide with those of the velocity potential,  $\phi$ , as defined by  $\mathbf{u} = \nabla\phi$ . The



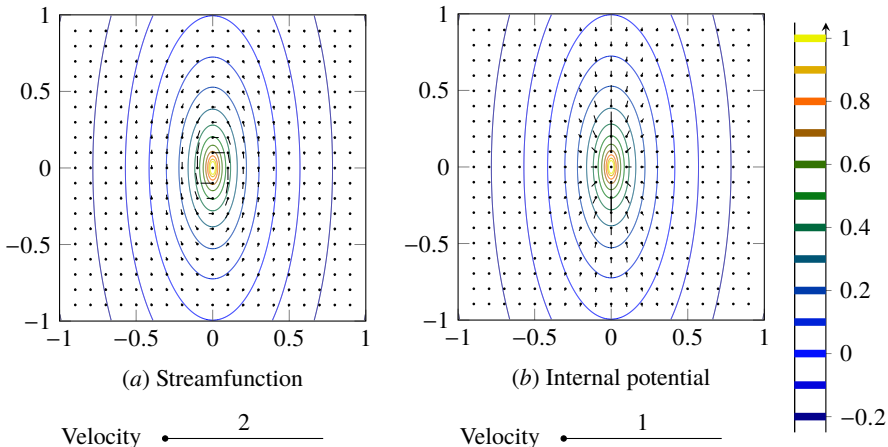


Figure 2: Real component of the evanescent Green's function for  $\omega = 1.1N$ , which shows (a) the streamlines and (b) contours of the internal potential, and the derived velocity fields at  $t = 0$ . The velocity indicators have been scaled for plotting. The potentials and their corresponding fluid speeds grow unboundedly at the origin. The imaginary part is identically zero.

262 fundamental streamfunction flow is a monochromatic point vortex, whereas for the internal  
 263 potential, it is a monochromatic volume source.

264 For  $|\omega| < N$ , we obtain propagating solutions with characteristics of gradient  $\pm 1/\gamma$ . The  
 265 imaginary part of the Green's function for  $\omega = 0.5N$  is plotted in figure 3. The real part is  
 266 piecewise constant with discontinuities across the characteristics. When  $|x - x_0| > \gamma|z - z_0|$ ,  
 267 the real part equals  $1/(4\omega^2\gamma)$  and equals zero elsewhere. We see a St. Andrew's Cross pattern  
 268 analogous to that produced by a small cylinder undergoing vertical oscillations (Görtler  
 269 1943; Mowbray & Rarity 1967). The potential and derived velocities grow unboundedly on  
 270 approaching the characteristics, which is a consequence of the idealisations embedded in this  
 271 model. Nonetheless, when integrated over point sources of zero area, a finite contribution is  
 272 obtained in the same way that an integration over  $\delta$ -functions produces a finite integral, a  
 273 property we will exploit in §3.2.

274 For  $|\omega| < N$ , the logarithm can be decomposed into two characteristic coordinates,

$$275 \quad \eta_{\pm} = \left( \frac{x - x_0}{\gamma} \right) \mp (z - z_0), \quad (3.8)$$

276 such that the  $\eta_+$  characteristics have positive slope and  $\eta_-$  negative. The argument of the  
 277 logarithm,  $|r^2|$ , becomes a difference of squares because  $\Gamma^2 < 0$ , so decomposes into the  
 278 characteristic coordinates,

$$279 \quad |r^2| = \left| \left[ \left( \frac{x - x_0}{\gamma} \right) - (z - z_0) \right] \left[ \left( \frac{x - x_0}{\gamma} \right) + (z - z_0) \right] \right| = |\eta_+ \eta_-|. \quad (3.9)$$

280 Therefore, the logarithm splits into two linearly superposed components with no cross term,

$$281 \quad \log |r^2| = \log |\eta_+| + \log |\eta_-|. \quad (3.10)$$

282 The solution to a cylinder undergoing small vertical oscillations shares this decoupling into  
 283  $\eta_{\pm}$  components (Hurley 1997). In the critical limit  $\omega \rightarrow N$  from below, the characteristics  
 284 are vertical, which smoothly transition to the ellipses of contours with infinite aspect ratio in  
 285 the limit  $\omega \rightarrow N$  from above.

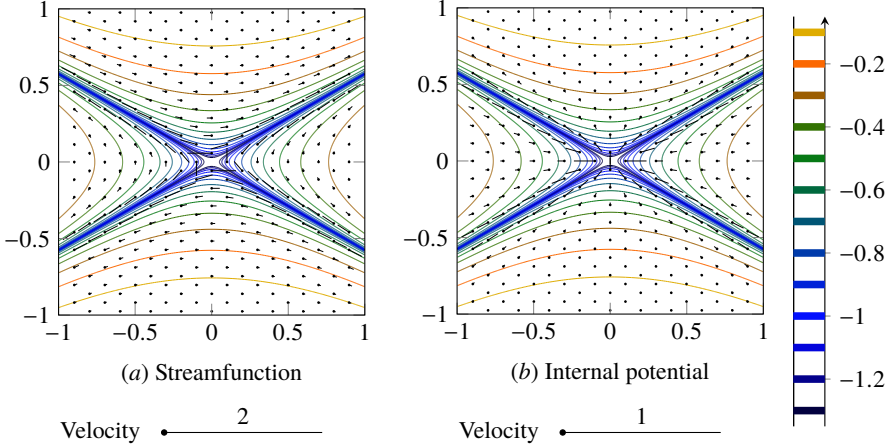


Figure 3: Imaginary component of the propagating Green’s function for  $\omega = 0.5N$ , which shows (a) the streamlines and (b) contours of the internal potential, and the derived velocity fields at time  $t = \pi/(2\omega)$ . The velocity indicators have the same scale as those in the evanescent case (figure 2). The potentials and corresponding fluid speeds grow unboundedly at the characteristics, with the largest ones, which would only be visible near the origin, omitted for clarity. The real part is zero in the regions above both characteristics and below both characteristics, and is  $1/(4\omega^2\gamma)$  in the remaining regions to the left of both characteristics and to the right of both characteristics.

286

### 3.2. Numerical implementation

287

288

289

290

291

292

293

294

295

296

297

298

In §3.1, we derived the Green’s function for continuous independent variables and then provided an integral formula for  $\chi_\omega$  over the distribution of point sources (3.2) that is not tractable to compute analytically. We now seek to use our Green’s function solution as the basis for a semi-analytical method to evaluate the potential,  $\chi_\omega$ , at arbitrary locations in space. We anticipate distributed sources, so the potential strength at any evaluation point in space will be composed of a linear superposition of solutions from all sources. Unfortunately, our solution has logarithmic singularities along the characteristics, and so any numerical method based on pointwise evaluation will suffer from unresolvable infinities. However, with careful treatment we may regularise these over finite integration elements, and thus we discretise the domain into elements of size  $\Delta x \Delta z$ . We account for the effect of integrating over an element by introducing a corresponding modified discrete Green’s function,  $G_D(\mathbf{x}; \mathbf{x}_D)$ , and source distribution,  $f_D(\mathbf{x}_D)$ , where the centres of such elements are at  $\mathbf{x}_D$ , so that

299

$$\chi_\omega(\mathbf{x}) = \sum_{\mathbf{x}_D} G_D(\mathbf{x}; \mathbf{x}_D) f_D(\mathbf{x}_D). \quad (3.11)$$

300

301

302

303

304

305

306

307

308

309

While much of what follows is required to determine  $G_D$ , we may simply take  $f_D(\mathbf{x}_D) = (1/(\Delta x \Delta z)) \iint f_\omega(\mathbf{x}_0) d^2\mathbf{x}_0$ , integrated over the element. For smooth source distributions, we make the approximation  $f_D(\mathbf{x}_D) \approx f_\omega(\mathbf{x}_D)$ . If instead there is an isolated  $\delta$ -function source of strength  $q$  that lies somewhere within the element, the mean source density is  $f_D = q/(\Delta x \Delta z)$ . Correspondingly, a smooth line source distribution of the form  $f_\omega = q(x) \delta(z - z_0)$  has mean density  $f_D \approx q(x_D)/\Delta z$ .

We note in passing that a transformed coordinate system in  $(\eta_+, \eta_-)$  aligns with the characteristic directions of propagating waves,  $|\omega| < N$ , but no single coordinate system would be optimal for a polychromatic wave field as highlighted in §4. Thus, we opt to discretise a regular Cartesian grid in  $(x, z)$ .

310 The Green's function only depends on the displacement from the source to the evaluation  
 311 point, so by moving the reference frame to the centre of the finite element enclosing the  
 312 source,  $\mathbf{x}_D$ , we may define a continuous variable  $\mathbf{x}' = \mathbf{x} - \mathbf{x}_D$  over which we may integrate  
 313 to determine  $G_D$  for all elements. Since the grid is regular, then for a given frequency we only  
 314 need to calculate the Green's function once for each relative displacement. Then, we translate  
 315 the resulting array of values according to  $\mathbf{x}_D$  when evaluating the summation for  $\chi_\omega$  (3.11),  
 316 truncating any values that fall outside the numerical domain.

317 We choose approximate formulae for each element in the Green's function matrix,  $G_D$ ,  
 318 according to the classification in figure 4. The figure only shows elements in the first quadrant,  
 319 with the other quadrants deduced by symmetry. In the remainder of this section, we explain  
 320 the decision points and formulae referenced in the figure.

321 Except at the source and elsewhere near its characteristics, the continuous Green's function  
 322 is regular and may be approximated by a Riemann sum of the form

$$323 \quad G_D(\mathbf{x}; \mathbf{x}_D) \approx G_\omega(\mathbf{x}; \mathbf{x}_D) \Delta x \Delta z. \quad (3.12)$$

324 For  $|\omega| > N$ , the only singular element is that which encloses  $\mathbf{x}' = \mathbf{0}$ , and in this case the  
 325 integral is given by

$$326 \quad G_D(\mathbf{x}_D; \mathbf{x}_D) = \int_{-\Delta x/2}^{\Delta x/2} \int_{-\Delta z/2}^{\Delta z/2} -\frac{\log\left(\left(\frac{x'}{\Gamma}\right)^2 + z'^2\right)}{4\pi\omega^2\Gamma} dz' dx'. \quad (3.13)$$

327 The dominant contribution to the integral comes from the logarithm close to the singularity,  
 328 so we approximate the integral on the rectangular element by an ellipse of equivalent area.  
 329 After dilatation, the radius,  $R$ , of the resulting circle is given by  $\pi R^2 = \Delta x \Delta z / \Gamma$ . We  
 330 re-express the Green's function in polar coordinates,

$$331 \quad G_D(\mathbf{x}_D; \mathbf{x}_D) \approx \int_0^{2\pi} \int_0^R -\frac{\log(r^2)}{4\pi\omega^2\Gamma} r dr d\theta. \quad (3.14)$$

332 Integration by parts gives

$$333 \quad G_D(\mathbf{x}_D; \mathbf{x}_D) \approx \frac{\Delta x \Delta z}{4\pi\omega^2\Gamma^2} \left(1 - \log \frac{\Delta x \Delta z}{\pi\Gamma}\right). \quad (3.15)$$

334 For the case where internal waves may be generated,  $|\omega| < N$ , the imaginary part of the  
 335 Green's function decomposes into the sum of two linearly independent components (3.10),  
 336 one for each characteristic direction. Using symmetry, singular elements along the  $x'$  or  
 337  $z'$  axes intersect both characteristics (the case of two characteristics in figure 4). Conversely,  
 338 singular elements away from the axes may only intersect one characteristic. We calculate each  
 339  $\eta_\pm$  component of  $G_D$  separately and then add them together. For elements significantly away  
 340 from the corresponding characteristic,  $\eta_\pm = 0$ , the component of the Green's function varies  
 341 approximately linearly across the element and we invoke the centre-value approximation for  
 342 a regular point (3.12). Otherwise, when the characteristic passes through an element or close  
 343 to one of its corners, we approximate this component of  $G_D$  using integrals as follows.

344 Let us consider the  $\eta_+$  component for a singular element, and define  $\eta_R$  and  $\eta_L$  to be  
 345 the maximum and minimum values respectively of  $\eta_+ = x'/\gamma - z'$  in this element. The  
 346 displacement of the element,  $\mathbf{x}'$ , is defined by the position of its centre. Because the level  
 347 sets of  $\eta_+$  are lines of positive gradient and  $\eta_+$  is increasing in  $x'$ , the maximum value of  $\eta_+$

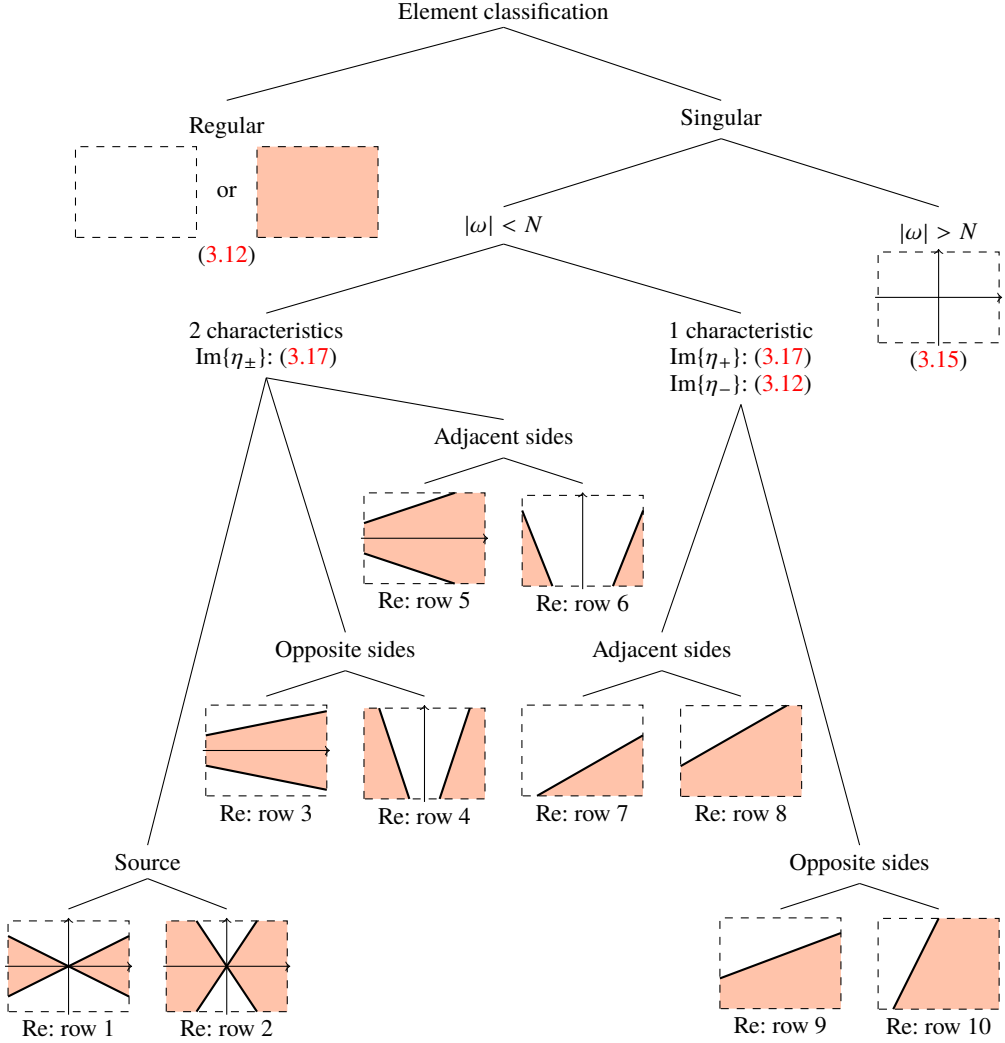


Figure 4: Classification of finite element types in the first quadrant showing the breakdown according to whether  $G_\omega$  remains finite within the element, whether propagating or evanescent and by the geometry of the intersections between characteristics and the element boundary. The thumbnail images show  $\text{Re}\{G_\omega\}$ , which equals  $1/(4\omega^2\gamma)$  in the shaded regions and zero elsewhere. Formulae for evaluating  $G_D$  are given for each case, and the areas for calculating  $\text{Re}\{G_D\}$  in the propagating case are referenced by their row numbers in table 1.

348 occurs in the bottom-right corner of the element and the minimum in the top-left corner, so

$$349 \quad \eta_R = \eta_+ \left( x' + \frac{\Delta x}{2}, z' - \frac{\Delta z}{2} \right) = \frac{x' + \frac{\Delta x}{2}}{\gamma} - \left( z' - \frac{\Delta z}{2} \right), \quad (3.16a)$$

$$350 \quad \eta_L = \eta_+ \left( x' - \frac{\Delta x}{2}, z' + \frac{\Delta z}{2} \right) = \frac{x' - \frac{\Delta x}{2}}{\gamma} - \left( z' + \frac{\Delta z}{2} \right). \quad (3.16b)$$

352 We approximate the contribution across the element by integrating over a rectangle aligned  
 353 with the characteristic that intersects the element corners where  $\eta_+ = \eta_R$  and  $\eta_+ = \eta_L$ , and

355 then scale the value by the ratio of areas. The contribution to  $G_D$  is approximately

$$\begin{aligned}
 & \left( \frac{\Delta x \Delta z}{|\eta_R - \eta_L|} \right) \left( \frac{i}{4\pi\omega^2\gamma} \int_{\eta_L}^{\eta_R} \log |\eta_+| d\eta_+ \right) \\
 356 & = \left( \frac{\Delta x \Delta z}{|\eta_R - \eta_L|} \right) \left( \frac{i}{4\pi\omega^2\gamma} \right) (\eta_R (\log |\eta_R| - 1) - \eta_L (\log |\eta_L| - 1)), \quad (3.17)
 \end{aligned}$$

357 after integration by parts, where we clarify that  $\eta \log \eta = 0$  when  $\eta = 0$ . By symmetry, the  
 358 same expression holds for the singular contribution due to  $\eta_-$  terms.

359 This leaves the real part of  $G_\omega$  to consider. It is only nonzero in the regions to the left  
 360 and to the right of the source bounded by the characteristics, which are shown for the first  
 361 quadrant as shaded regions in figure 4. The real part of the integral over the element is  
 362 given by  $1/(4\omega^2\gamma)$  multiplied by the shaded area. We present in table 1 the formulae for all  
 363 permutations of shaded area expressed in the  $\mathbf{x}'$  coordinate system centred on an element.

## 364 4. Application to aperiodic configurations

### 365 4.1. Introduction

366 Internal waves are frequently generated by moving boundaries. For example, in the laboratory,  
 367 McEwan (1971, 1973) used articulated paddles and Gostiaux *et al.* (2007) used rotating cams,  
 368 but these are best suited to monochromatic excitations. We installed a ‘‘magic carpet’’ (Dobra  
 369 *et al.* 2019) in the base of our tank, which has more general possibilities for excitation.  
 370 Likewise, we generalise our numerical method for a single frequency,  $\chi_\omega \exp(-i\omega t)$ ,  
 371 described in §3 to those that have a continuous spectrum of frequencies.

372 For a distribution of sources  $f(x, z, t) = \int f_\omega(x, z) \exp(-i\omega t) d\omega$ , we may write

$$373 \quad \chi(\mathbf{x}, t) = \int_{\mathbb{R}} \exp(-i\omega t) \iint_{\mathbb{R}^2} G_\omega(\mathbf{x}; \mathbf{x}_0) f_\omega(\mathbf{x}_0) d^2\mathbf{x}_0 d\omega. \quad (4.1)$$

374 Our numerical method allows replacement of these integrals with the discrete Fourier  
 375 transform, and thus we may approximate general wave fields. We summarise our procedure  
 376 in algorithm 1. In the special case of a discrete set of input frequencies, we no longer need  
 377 to resolve the Fourier transform and all the frequencies can be represented exactly.

378 In our model, we consider flexible boundaries as sources of either volume or vorticity.  
 379 As we saw in §2, source terms in the internal wave equation for internal potential and  
 380 streamfunction represent volume and vorticity sources respectively. We now derive formulae  
 381 for the source terms of both potentials,  $\xi$  and  $\psi$ , to describe each temporal mode of an  
 382 arbitrary vertical displacement of a horizontal boundary.

### 383 4.2. Representing active boundaries with finite element sources

384 In both cases, we can readily derive volume fluxes for a monochromatic source of unit strength  
 385 by integrating the Green’s function, so we rescale these fluxes to match a discrete physical  
 386 representation of a short distance along the boundary. The rescaling factors are collectively  
 387 the required distribution of sources along the entire length of the boundary. Here, we outline  
 388 the method and summarise key results; see §§4.2.1–4.2.2 for full derivations. Throughout this  
 389 section, all sources are at the zero-height of the magic carpet, so without loss of generality  
 390 we take  $z_0 = 0$ .

391 We seek to determine the volume flux,  $Q(t) = Q_\omega \exp(-i\omega t)$ , induced by a monochromatic  
 392 source of unit strength across a transect of the domain. For the internal potential, the transect  
 393 is a horizontal line at  $z > 0$  ranging from  $x = -\infty$  to  $+\infty$ , across which the flux amplitude  
 394  $Q_\omega = \frac{1}{2}$ . Whereas, the corresponding transect for the streamfunction is a vertical line segment

Case	Criterion	Shaded area
1	$\mathbf{x}' = \mathbf{0}$ $\Delta x \leq \gamma \Delta z$	$\frac{(\Delta x)^2}{2\gamma}$
2	$\mathbf{x}' = \mathbf{0}$ $\Delta x > \gamma \Delta z$	$\Delta x \Delta z - \frac{\gamma(\Delta z)^2}{2}$
3	$x' \neq 0, z' = 0$ $ x'  + \frac{\Delta x}{2} \leq \gamma \frac{\Delta z}{2}$	$\frac{2 x' \Delta x}{\gamma}$
4	$x' = 0, z' \neq 0$ $\frac{\Delta x}{2} \geq \gamma( z'  + \frac{\Delta z}{2})$	$\Delta x \Delta z - 2\gamma z' \Delta z$
5	$x' \neq 0, z' = 0$ $ x'  - \frac{\Delta x}{2} \leq \gamma \frac{\Delta z}{2}$ $ x'  + \frac{\Delta x}{2} > \gamma \frac{\Delta z}{2}$	$\Delta x \Delta z - \frac{1}{\gamma} \left(  x'  - \frac{\Delta x}{2} - \gamma \frac{\Delta z}{2} \right)^2$
6	$x' = 0, z' \neq 0$ $\frac{\Delta x}{2} \geq \gamma( z'  - \frac{\Delta z}{2})$ $\frac{\Delta x}{2} < \gamma( z'  + \frac{\Delta z}{2})$	$\frac{1}{\gamma} \left( \frac{\Delta x}{2} - \gamma( z'  - \frac{\Delta z}{2}) \right)^2$
7	$x' \neq 0, z' \neq 0$ $ x'  - \frac{\Delta x}{2} \leq \gamma( z'  - \frac{\Delta z}{2})$ $ x'  + \frac{\Delta x}{2} \leq \gamma( z'  + \frac{\Delta z}{2})$	$\frac{1}{2\gamma} \left(  x'  + \frac{\Delta x}{2} - \gamma( z'  - \frac{\Delta z}{2}) \right)^2$
8	$x' \neq 0, z' \neq 0$ $ x'  - \frac{\Delta x}{2} > \gamma( z'  - \frac{\Delta z}{2})$ $ x'  + \frac{\Delta x}{2} > \gamma( z'  + \frac{\Delta z}{2})$	$\Delta x \Delta z - \frac{1}{2\gamma} \left(  x'  - \frac{\Delta x}{2} - \gamma( z'  + \frac{\Delta z}{2}) \right)^2$
9	$x' \neq 0, z' \neq 0$ $ x'  - \frac{\Delta x}{2} > \gamma( z'  - \frac{\Delta z}{2})$ $ x'  + \frac{\Delta x}{2} \leq \gamma( z'  + \frac{\Delta z}{2})$	$\frac{\Delta x}{\gamma} \left(  x'  - \gamma( z'  - \frac{\Delta z}{2}) \right)$
10'	$x' \neq 0, z' \neq 0$ $ x'  - \frac{\Delta x}{2} \leq \gamma( z'  - \frac{\Delta z}{2})$ $ x'  + \frac{\Delta x}{2} > \gamma( z'  + \frac{\Delta z}{2})$	$\Delta z \left(  x'  + \frac{\Delta x}{2} - \gamma z'  \right)$

Table 1: Shaded area of each type of singular element centred on  $\mathbf{x}'$ . These thumbnails are shown for quadrant 1; other quadrants are deduced by symmetry. It is helpful to observe that  $|x'| = \gamma|z'|$  on the characteristics. In cases 7–10, in addition to the given criteria, we explicitly require that a characteristic passes through the element: in the first and third quadrants, only the  $\eta_+$  characteristic may intersect the element, but in the second and fourth quadrants, only the  $\eta_-$  characteristic may intersect it. These areas are multiplied by  $1/(4\omega^2\gamma)$  to give  $\text{Re}\{G_D\}$ .

395 to the right of the wave maker ranging from  $z = 0$  to  $+\infty$ , across which  $Q_\omega = 1/(4\omega^2\gamma)$ . In  
 396 both cases, we find that the component of the Green's function flow satisfying the conditions  
 397 imposed by the physical model of the magic carpet is in phase with the forcing,  $\text{Re}\{Q_\omega\}$ , and  
 398 are line jets along the characteristics, which can be represented by  $\delta$ -functions.

**Input:**  $f(\mathbf{x}, t)$ ,  $N$

**Result:**  $\chi(\mathbf{x}, t)$

$\chi \leftarrow 0$

**for**  $\omega \in \mathbb{R}$  **do**

$f_D(\mathbf{x}) \leftarrow \frac{\Delta t}{2\pi} \sum_t f(\mathbf{x}, t) \exp(i\omega t)$

    // Calculate discrete Green's function using figure 4

$G_D \leftarrow \text{table}(2N_x - 1, 2N_z - 1)$  // Set up lookup table

**foreach**  $(i, j) \in G_D$  **do**

**if** *Regular element* **then**  $G_D(i, j) = (3.12)$

**else** // Singular element

**if**  $|\omega| > N$  **then**  $G_D(i, j) = (3.15)$

**else** //  $|\omega| < N$

**foreach** *Characteristic* **do**

**if** *Element intersection* **then**  $\text{Im}\{G_D(i, j)\} = (3.17)$

**else**  $\text{Im}\{G_D(i, j)\} = (3.12)$

**end**

$\text{Re}\{G_D(i, j)\} = \frac{1}{4\omega^2\gamma} \times (\text{shaded area: table 1})$

**end**

**end**

**end**

    // Sum over sources according to (3.11)

$\chi_\omega \leftarrow \text{table}(N_x, N_z)$

**foreach**  $(k, l) \in \chi_\omega$  **do**

$\chi_\omega(k, l) \leftarrow 0$

**foreach**  $(i, j) \in f_D$  **do**

$\chi_\omega(k, l) \leftarrow \chi_\omega(k, l) + G_D(N_x + k - i, N_z + l - j) f_D(i, j)$

**end**

**end**

$\chi \leftarrow \chi + \chi_\omega \exp(-i\omega t)$

**end**

ALGORITHM 1. Calculation of potential  $\chi$  for an arbitrary source distribution  $f(\mathbf{x}, t)$ . It is calculated mode-by-mode using the discrete monochromatic Green's function,  $G_D$ . At each frequency, we first evaluate  $f_D$  and  $G_D$ , then finally we accumulate contributions to the potential field.

399 The total volume flux from one finite grid element of width  $\Delta x$  and height  $\Delta z$  that  
400 is centred on  $(x_0, 0)$  and contains the distribution of monochromatic point sources  $f =$   
401  $f_\omega(x, z) \exp(-i\omega t)$  is

$$\int_{x_0 - \Delta x/2}^{x_0 + \Delta x/2} \int_{-\Delta z/2}^{\Delta z/2} Q_\omega f_\omega(x', z') \exp(-i\omega t) dz' dx' \approx \Delta x \Delta z Q_\omega f_\omega(x_0, 0) \exp(-i\omega t). \quad (4.2)$$

402

403 Then, we equate this expression with the corresponding volume flux,  $R(t) = R_\omega \exp(-i\omega t)$ ,  
404 predicted by a physical model of volume displacement by the wave maker surface to obtain  
405 the distribution of sources,

406

$$f_\omega(x_0, 0) = \frac{R_\omega}{\Delta x \Delta z Q_\omega}. \quad (4.3)$$

407 For the internal potential,  $R_\omega = -i\omega\Delta x h_\omega(x_0)$ , so  $f_\omega(x_0, 0) = -(2i\omega/\Delta z) h_\omega(x_0)$ .  
 408 Whereas, for the streamfunction,  $R_\omega = -(i\omega\Delta x/2) h_\omega(x_0)$ , so  $f_\omega(x_0, 0) = -(2i\omega^3\gamma/\Delta z) h_\omega(x_0)$ .

409 4.2.1. Internal potential

410 For the internal potential, we determine the total vertical volume flux through a line of  
 411 constant  $z \neq 0$ ,

$$412 \quad Q(z, t) = Q_\omega(z) \exp(-i\omega t) = \int_{-\infty}^{\infty} w(x, z, t) dx, \quad (4.4)$$

413 for the Green's function when  $0 < \omega < N$ . The vertical velocity field,  $w$ , is given by  
 414  $\partial^3(G_\omega \exp(-i\omega t))/\partial t^2 \partial z$  and thus  $w = -\omega^2 (\partial G_\omega/\partial z) \exp(-i\omega t)$ . Applying the chain  
 415 rule to  $G_\omega$  (3.7) when  $z_0 = 0$ , we obtain

$$416 \quad \frac{\partial G_\omega}{\partial z} = -i \frac{z}{2\pi\omega^2\gamma \left[ \left( \frac{x-x_0}{\gamma} \right)^2 - z^2 \right]} - \frac{z}{2\omega^2\gamma} \delta \left( \left( \frac{x-x_0}{\gamma} \right)^2 - z^2 \right). \quad (4.5)$$

417 Along a path of constant  $z$  (where  $z \neq 0$ ) as shown in figure 5, the imaginary part has two  
 418 simple poles,  $x = x_0 \pm \gamma z$ , which are where the path crosses the characteristics of  $G_\omega$ , and  
 419  $\partial G_\omega/\partial z$  asymptotes inverse-linearly towards them. Between the poles (in the line segment  
 420 containing  $x = x_0$ ),  $\text{sgn}(\text{Im}\{\partial G_\omega/\partial z\}) = +\text{sgn}(z)$ , and outside the poles (where  $x \rightarrow \pm\infty$ ),  
 421  $\text{sgn}(\text{Im}\{\partial G_\omega/\partial z\}) = -\text{sgn}(z)$ . Thus, we may use the Cauchy principle value to regularise  
 422  $Q_\omega$  at each pole. The imaginary part exhibits even symmetry about  $x = x_0$ , so it suffices to  
 423 consider only half of the domain and double the result,

$$424 \quad \text{Im}\{Q_\omega(z)\} = \lim_{\epsilon \rightarrow 0} \left\{ \frac{z}{\pi\gamma} \left( \int_{x_0}^{x_0+\gamma z-\epsilon} \frac{dx}{\left( \frac{x-x_0}{\gamma} \right)^2 - z^2} - \int_{x_0+\gamma z+\epsilon}^{\infty} \frac{dx}{\left( \frac{x-x_0}{\gamma} \right)^2 - z^2} \right) \right\}. \quad (4.6)$$

425 Factoring out  $z^2$  and using the substitution  $p = (x - x_0)/(\gamma z)$  leaves

$$426 \quad \text{Im}\{Q_\omega(z)\} = \lim_{\epsilon \rightarrow 0} \left\{ \frac{1}{\pi} \left( \int_0^{1-\epsilon/(\gamma z)} \frac{dp}{p^2 - 1} - \int_{1+\epsilon/(\gamma z)}^{\infty} \frac{dp}{p^2 - 1} \right) \right\}. \quad (4.7)$$

427 The scaling on the limit variable,  $\epsilon$ , is the same for both integrals, so we may replace the  
 428 corresponding limits on the integrals by  $1 \mp \epsilon$ . Then, evaluating the definite integrals yields

$$429 \quad \text{Im}\{Q_\omega(z)\} = \lim_{\epsilon \rightarrow 0} \left\{ \frac{1}{2\pi} \left( \left[ \log \frac{1-p}{1+p} \right]_0^{1-\epsilon} - \left[ \log \frac{p-1}{p+1} \right]_{1+\epsilon}^{\infty} \right) \right\} = 0. \quad (4.8)$$

430 Next, we consider the integral over the  $\delta$ -function in the real part. Along a path of constant  $z$ ,  
 431 the argument of the  $\delta$ -function has two simple zeroes,  $y_{1,2} = x_0 \pm \gamma z$ , for which we use the  
 432 standard formula,

$$433 \quad \delta(f(x)) = \sum_{k=1}^2 \frac{\delta(x - y_k)}{\left| \frac{df}{dx} \right|_{y_k}}. \quad (4.9)$$

434 Here,  $df/dx = 2(x - x_0)/\gamma^2$ , so we have

$$435 \quad \text{Re}\{Q_\omega(z)\} = \int_{-\infty}^{\infty} \frac{z}{2\gamma} \left( \frac{\delta(x - [x_0 + \gamma z])}{\left| \frac{2}{\gamma^2} \gamma z \right|} + \frac{\delta(x - [x_0 - \gamma z])}{\left| -\frac{2}{\gamma^2} \gamma z \right|} \right) dx. \quad (4.10)$$



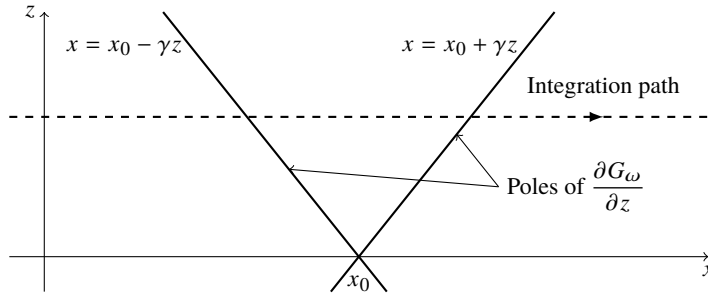


Figure 5: Integration path for calculating the volume flux,  $Q$ , for the internal potential, showing the locations of the poles in the imaginary part of  $\partial G_\omega / \partial z$ , which are also the locations of the singularities in the real part.

436 Each  $\delta$ -function contributes a value of one to the integral and  $z/|z| = \text{sgn}(z)$ , so  
 437  $\text{Re}\{Q_\omega(z)\} = \frac{1}{2} \text{sgn}(z)$ . Therefore,  $Q(z) = \frac{1}{2} \text{sgn}(z) \exp(-i\omega t)$ .

438 The total vertical volume flux through a horizontal transect is half the strength of the internal  
 439 potential point source and is in phase with the source. The flux has a vertical component  
 440 everywhere except  $z = 0$  and points away from the source when the source is positive.  
 441 Closing a rectangular contour along  $z = \pm z_0$  and  $x = \pm\infty$ , symmetry arguments determine  
 442 that the vertical integrals at  $x = \pm\infty$  are both zero and integration along the horizontal edges  
 443 doubles due to the direction in which they are taken. Thus, a monochromatic point source of  
 444 internal potential of unit strength forces the internal wave equation such that the total volume  
 445 flux is monochromatic and of unit strength.

446 We remark that this result also applies to a corresponding integral when the Green's  
 447 function is for the streamfunction,

$$448 \int_{-\infty}^{\infty} -u \, dx = \int_{-\infty}^{\infty} \frac{\partial G_\omega}{\partial z} \, dx = \frac{1}{2} \text{sgn}(z) \exp(-i\omega t). \quad (4.11)$$

449 Using the same rectangular contour, we obtain the circulation around the point source to  
 450 be  $\frac{1}{2} \exp(-i\omega t)$ . Letting  $z \rightarrow 0$  so that the area enclosed in the contour tends to zero and  
 451 invoking Stokes' theorem shows that the source is a point vortex of strength  $\frac{1}{2} \exp(-i\omega t)$ .

452 Similar to a resonant simple harmonic oscillator, there are components of the internal  
 453 potential field both in phase to the forcing and with a phase lag of a quarter oscillation behind  
 454 the source. Here, the in-phase response ensures the conservation of volume by generating  
 455 line jets only and exactly along the characteristics, while the phase-lagged response has zero  
 456 net volume flux despite inducing a flow over the whole domain.

457 Physically modelling the wave maker, the upwards volume flux generated by an element  
 458 with vertical displacement  $h$ , as shown in figure 6, is

$$459 R(t) = \int_{x_0 - \Delta x/2}^{x_0 + \Delta x/2} \frac{\partial h}{\partial t} \, dx', \quad (4.12)$$

460 which is approximately equal to  $-i\omega \Delta x h_\omega \exp(-i\omega t)$  for small elements. Substituting this  
 461 into the formula for the required element source strength (4.3) yields the required source  
 462 strengths for use in the discrete Green's function,  $f_\omega(x_0, 0) = -(2i\omega/\Delta z) h_\omega(x_0)$ .

#### 463 4.2.2. Streamfunction

464 When the Green's function represents the streamfunction, the volume flux across any  
 465 horizontal or vertical transect is zero, because sources in the streamfunction internal wave  
 466 equation are vortices. Instead, since the volume flux across a path is equal to the difference

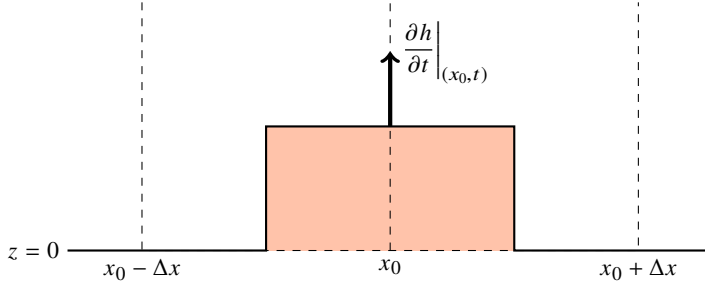


Figure 6: Finite element of width  $\Delta x$  representing wave maker displacement at a single location. We use this model to calculate the induced vertical volume flux required for sources to the internal potential, which is  $\Delta x \partial h / \partial t|_{(x_0,t)}$ . The vertical dashed lines indicate the element centrelines.

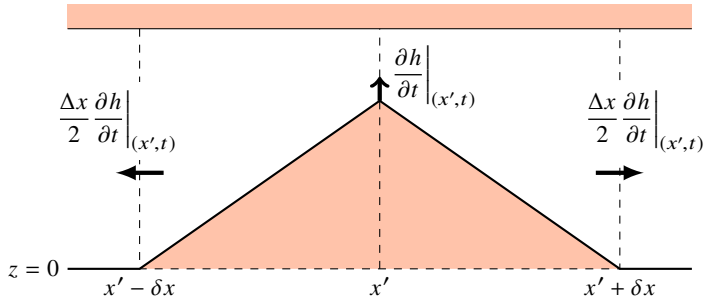


Figure 7: Infinitesimal element representing wave maker displacement at a single location, assuming the profile to be linear between sample points  $\delta x$  apart and the domain to have a rigid lid. We use this model to calculate along-wave maker gradients of induced horizontal volume flux, whose integrals are required for finite sources of width  $\Delta x$  to the streamfunction.

467 between the values of the streamfunction at each end, we note that the real part of the volume  
 468 flux induced by  $G_\omega$  (3.7) across any semi-infinite vertical line from  $z = 0$  to  $z = \infty$   
 469 constant  $x$  is  $Q_\omega = 1/(4\omega^2\gamma)$ . The point vortex is in phase with the source, so it is not  
 470 necessary to consider the imaginary part.

471 For the physical model, we consider a wave maker profile that is spatially sampled every  $\delta x$   
 472 and is zero everywhere except at one sample point,  $x = x'$ , as shown in figure 7. We  
 473 assume that the wave maker is piecewise linear between the sample points. The rightwards  
 474 volume flux generated to the right of the displaced infinitesimal element is  $R(x' + \delta x, t) =$   
 475  $(\Delta x/2) \partial h / \partial t|_{(x',t)}$ . Conversely, the rightwards volume flux to the left of the element is  
 476  $R(x' - \delta x, t) = -(\Delta x/2) \partial h / \partial t|_{(x',t)}$ . In the continuum limit, we have

$$477 \quad \left. \frac{\partial R}{\partial x} \right|_{(x',t)} = \lim_{\delta x \rightarrow 0} \frac{R(x' + \delta x, t) - R(x' - \delta x, t)}{2 \delta x} = \frac{1}{2} \left. \frac{\partial h}{\partial t} \right|_{(x',t)}. \quad (4.13)$$

478 Integrating such point contributions over a finite element of width  $\Delta x$  centred on  $(x_0, 0)$  gives  
 479 the total horizontal volume flux across one source element,

$$480 \quad R(x_0, t) = \int_{x_0 - \Delta x/2}^{x_0 + \Delta x/2} \frac{1}{2} \frac{\partial h}{\partial t} dx \approx \frac{\Delta x}{2} \left. \frac{\partial h}{\partial t} \right|_{(x_0,t)}, \quad (4.14)$$

481 to leading order in  $\Delta x$ . Thus,  $R_\omega = -(\mathrm{i}\omega\Delta x/2) h_\omega(x_0)$  and  $f_\omega(x_0, 0) = -(2\mathrm{i}\omega^3\gamma/\Delta z) h_\omega(x_0)$ .

## 4.3. Boundary considerations

482

483 Nonzero-frequency internal waves in a finite domain will inevitably reflect off the top and  
 484 bottom. In both cases, the fluid cannot flow across the boundary, so we take  $w = 0$  as the  
 485 boundary condition and exploit the characteristic structure of internal waves to enforce it.  
 486 The required potential,  $\chi$ , for the reflected wave is calculated along the boundary and then  
 487 projected along its characteristics using an approach introduced in Dobra *et al.* (2021). The  
 488 characteristics of the reflected wave are oriented in the opposite vertical, but same horizontal,  
 489 direction as the incident wave.

490

491 For the internal potential in a monochromatic flow,  $w = -\omega^2 \partial \xi / \partial z$  and on the boundary,  
 492 the reflected wave may take the same value of the internal potential as the incident wave.  
 493 By contrast, the vertical velocity is obtained from the streamfunction as  $w = \partial \psi / \partial x$ , giving  
 494  $\psi = \text{const.}$  on the boundary, so we require that the reflected streamfunction is the negative  
 495 of the incident. In both cases, we set the gauge constant to zero for convenience.

495

496 Evaluating  $\chi$  only on the boundary is insufficient to deduce the horizontal direction of  
 497 incident characteristics. A wave field of a particular frequency may contain waves in all  
 498 directions, so we use a principal axes transformation to decompose the incident wave field  
 499 into left- and right-travelling waves according to the direction of the gradient vector (Dobra  
 2018, pp. 37–39) and reflect each component in turn.

500

501 The interference pattern arising from the distribution of sources generates the desired  
 502 wave field, but where the source array is abruptly truncated, powerful harmonics are emitted  
 503 and they may contaminate the solution within the domain. To reduce the severity of such  
 504 truncation, we smoothly reduce the source strength to zero at the lateral extremities of the  
 505 calculation domain according to a  $C^3$ -continuous ramp that extends well beyond the field of  
 506 view. Similarly, we use a significantly extended temporal domain for the Fourier transform  
 to avoid periodic reflection in time activity that is aperiodic and short in duration.

507

## 4.4. Experimental method

508 The Arbitrary Spectrum Wave Maker (ASWaM, Dobra *et al.* 2019) is a flexible section  
 509 1 m long and flush with the base of a tank that is 11 m long, 0.255 m wide and 0.48 m deep.  
 510 The magic carpet's shape is controlled by an array of 100 linear stepper motors positioned  
 511 at a pitch of 10 mm, each with a vertical resolution of 0.0127 mm and a stroke of 48 mm.

512

513 The surface of the wave maker is a nylon-faced neoprene foam sheet of thickness 3 mm.  
 514 The material has some resistance to bending, but the attachment mechanism is designed to  
 515 minimise the tensile stress in the sheet and the bending moments on the actuating rods. We  
 model the surface deformations at each instant,  $h(x, t)$ , as satisfying

516

$$\frac{Es^3}{12} \frac{\partial^4 h}{\partial x^4} - T \frac{\partial^2 h}{\partial x^2} = p_*, \quad (4.15)$$

517

518 where  $E$  is Young's modulus,  $s$  is the sheet thickness,  $T$  is the longitudinal tension in the  
 519 sheet and  $p_*$  is the pressure difference across the sheet, normally taken as zero. Defining  
 520  $\lambda = (12T/(Es^3))^{1/2}$ , this equation has eigensolutions  $\mathbf{f}(x) = [1 \ x \ \cosh \lambda x \ \sinh \lambda x]^T$ .  
 521 For our magic carpet, we find that  $\lambda \approx 400$ . These solutions differ from the typical Euler–  
 522 Bernoulli linear beam by the presence of hyperbolic functions instead of cubic polynomials,  
 523 and these differences arise from longitudinal tension. Defining a vector of constants  $\mathbf{b}$  to  
 524 be determined by the rod heights and enforcing  $C^2$ -continuity, the general solution between  
 525 each rod is  $h(x) = \mathbf{b} \cdot \mathbf{f}(x)$ . Combining the boundary conditions for all sections of the wave  
 526 maker gives a linear system of equations with constant coefficients, which can be easily  
 inverted numerically.

527

We fill the tank using the double bucket method (Fortuin 1960; Oster 1965) with a linear

528 density stratification in brine producing a constant buoyancy frequency  $N = 1.45 \text{ rad s}^{-1}$ .  
 529 We observe density perturbations using Synthetic Schlieren, an optical technique (Dalziel  
 530 *et al.* 1998; Sutherland *et al.* 1999; Dalziel *et al.* 2000). A static, random pattern of black  
 531 and white dots is displayed on a 4k (UHD) television screen measuring 1.4 m (55") on the  
 532 diagonal that is 0.2 m behind the tank, following Sveen & Dalziel (2005). The light rays  
 533 emitting from the screen bend as they pass through the varying refractive indices in the tank,  
 534 and the distorted images are recorded at 4 fps on a 12-megapixel ISVI IC-X12CXP video  
 535 camera located 3.8 m in front of the tank. A pattern-matching algorithm in the software  
 536 package DigiFlow (Dalziel Research Partners 2018) is used to reconstruct the gradient of the  
 537 density perturbation from the recorded images, and we plot its horizontal component, which  
 538 is related to the internal potential according to  $(1/\rho_{00}) \partial \rho' / \partial x = (N^2/g) \partial^3 \xi / \partial x \partial z \partial t$ .

#### 539 4.5. An example: atmospheric lee waves

540 A travelling solitary hump is perhaps the simplest aperiodic waveform, directly analogous  
 541 to flow over an isolated mountain ridge (Dalziel *et al.* 2011). In our experiments, the fluid  
 542 is stationary in the tank, so boundary layers do not form upstream and we obtain cleaner  
 543 waveforms.

544 We seek to validate our numerical model in this configuration, and we choose to calculate  
 545 the wave field using the internal potential, although we could equally obtain the same wave  
 546 field using the streamfunction. Our hump consists of a complete wavelength of a sinusoid  
 547 ranging from trough to trough, where the troughs are flush with the zero height of the  
 548 magic carpet, with wavelength 0.081 m and peak-to-trough amplitude 0.028 m propagating  
 549 to the right at  $U = 0.0357 \text{ m s}^{-1}$ . We use 1024 points spanning 50 s for the discrete Fourier  
 550 transform, giving a frequency resolution of  $0.13 \text{ rad s}^{-1}$ . The hump takes 2.3 s to pass any  
 551 fixed location, which corresponds to a frequency of  $2.8 \text{ rad s}^{-1}$ . With this adequate temporal  
 552 resolution, we thus avoid spurious reflections in the time domain.

553 The passing time of the hump corresponds to a frequency ratio of  $\omega/N = 1.88$ , which  
 554 is evanescent. Thus, it is clear that in this case the propagating modes will arise only from  
 555 peripheral harmonics in the spectrum, an observation to which we will return in §5. Figure 8  
 556 compares our experiments with the wave train predicted by our model.

557 Firstly, from selective withdrawal of modes in our numerical prediction, we deduce that  
 558 there are significant evanescent modes local to the hump, whose interference pattern is  
 559 required to capture the structure of the wave train observed in the experiment.

560 Secondly, we see disturbances spread across the domain, both in front and behind the  
 561 hump. The waves ahead of the hump appear to be quasi-stationary and persist in the observed  
 562 timeframe between six and eleven passing periods of the hump after its release. We conclude  
 563 that these are not simply startup transients, and so we use geometric reasoning to understand  
 564 the distribution of wave energy in the system.

565 One common approach is to use the principle of stationary phase (e.g. Lighthill 1978)  
 566 to restrict our analysis to elements of the wave field that move in phase with the hump.  
 567 The solitary hump may be characterised as a broadband spectrum of modes all travelling  
 568 with a common horizontal phase velocity,  $\omega/k = U$ . It follows that for a given range of  
 569 wavenumbers,  $k$ , there must directly correspond a range of frequencies,  $\omega$ . Thus, any internal  
 570 wave propagation generated by the hump has no preferential direction but must share the  
 571 same horizontal component of phase velocity. The dispersion relation (2.7) constrains the  
 572 magnitudes of all such wavevectors to the circle  $|\mathbf{k}| = N/U$ . Consequently, for positive  
 573 frequencies and upwards propagation, only fourth-quadrant wavevectors remain, and their  
 574 corresponding group velocities point into the first quadrant. These modes comprise the  
 575 majority of the observed signal, and their superposition results in curved phase lines.

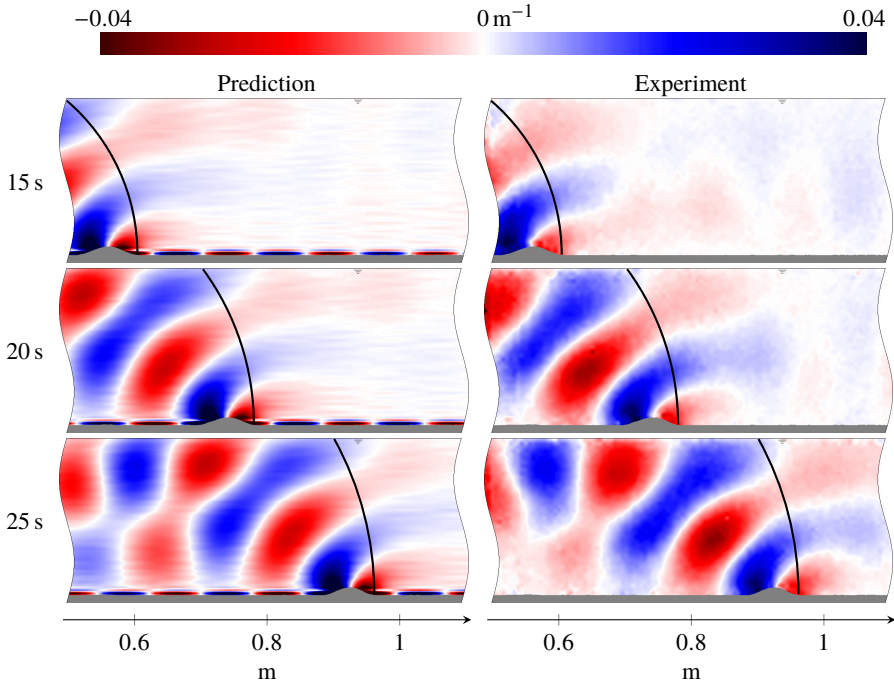


Figure 8: Prediction and experiment comparing  $(1/\rho_{00}) \partial \rho' / \partial x$  for a solitary sinusoidal hump of height 0.028 m and width 0.081 m moving at  $U = 0.0357 \text{ m s}^{-1}$ . Each image is separated by 5 s, and  $N = 1.45 \text{ rad s}^{-1}$ . The majority of the wave energy exists in waves phased-locked with the hump, and these waves are restricted to a semicircular envelope, indicated by the black arc. Wave energy to the right of the arc is carried by non-phase-locked waves, but whose spectrum results in a quasi-steady pattern of waves moving with the hump. There are also evanescent modes forming an interference pattern near the hump, but due to discretisation of the temporal spectrum in our prediction, some leakage of energy occurs along the wave maker surface but the response remains localised.

576 Furthermore, by following rays traced parallel to each mode's respective group velocity,  
 577 we may determine a propagation envelope for this class of quasi-steady wave. This envelope  
 578 forms a semicircle joining the hump's current and initial release locations (Dalziel *et al.*  
 579 2011), as shown by black arcs in figure 8. These advancing semicircles grow in radius until  
 580 the envelope asymptotically forms a vertical front.

581 Clearly, both the experiment and the prediction contain waves propagating ahead of this  
 582 envelope, so, as previously noted by Voisin (1994), the principle of stationary phase is  
 583 insufficient to account for the whole wave field. Given that there is signal high above the  
 584 wave maker and ahead of the hump, we deduce that these waves must have significant  
 585 vertical component to their group velocity and therefore have nonzero frequency. Moreover,  
 586 for internal waves the horizontal component of the group velocity is bounded above by the  
 587 horizontal component of the phase velocity, and any observable wave ahead of the hump  
 588 must have group velocity with horizontal component greater than  $U$ , so the same must also  
 589 be true for its phase velocity. Although counterintuitive, it is possible for a composition of  
 590 modes from a spectrum of phase velocities to form a quasi-steady wave field that translates  
 591 with a single apparent phase velocity. Akin to the decomposition of a standing wave into  
 592 opposing travelling waves, a carefully chosen difference of frequencies is sufficient to create  
 593 the required behaviour, although many combinations of wavevector and frequency would

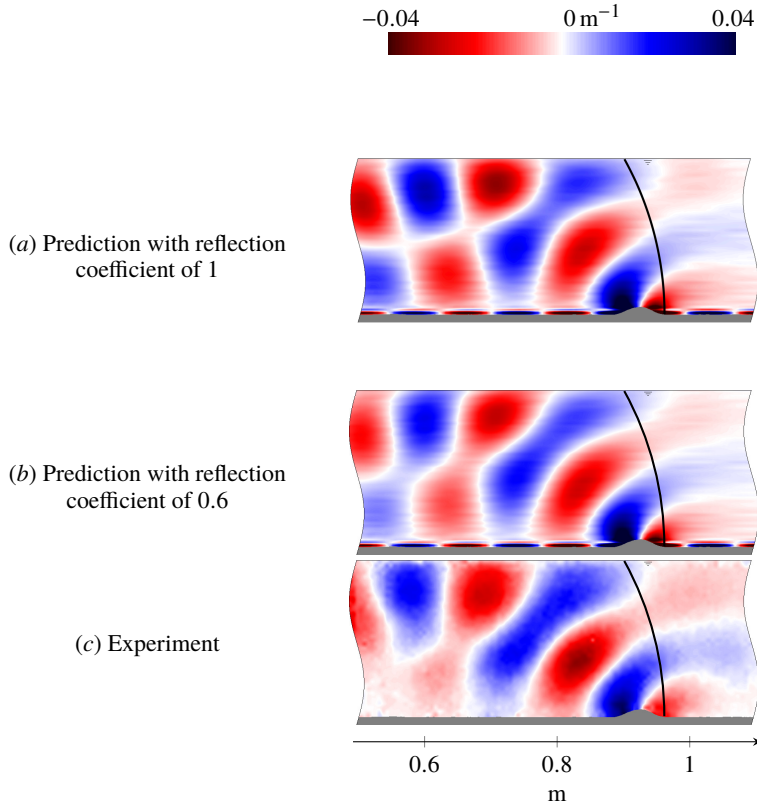


Figure 9: Predictions assuming pure reflections (a) and with calibrated attenuation at the free surface with coefficient 0.6 (b) compared to experiment (c). These correspond to figure 8 at 25 s and show  $(1/\rho_{00}) \partial \rho' / \partial x$ . Without attenuation, the predicted amplitude of the wave field behind the hump is larger than observed. The reflection coefficient accounts for energy dissipated at the free surface through mechanisms not directly modelled.

594 also produce an equivalent result. We conjecture that just such a superposition of modes is  
 595 responsible for propagation ahead of the envelope shown in figure 8.

596 We note that our approach requires the Fourier transform in time of the entire timeline.  
 597 Since the source strengths are zero at all times except when the hump is passing, the  $\omega$ -  
 598 spectrum is broad. However, a discrete Fourier transform introduces discretisation error,  
 599 which when inverted produces sources at unwanted times. We see their effect as forced  
 600 oscillations along the magic carpet, which have insignificant effect on the rest of the wave  
 601 field.

602 Our wave propagation model does not directly account for energy leaving the modelled  
 603 system during a reflection, yet is present in the experiments. We employed a line-search  
 604 optimisation to determine suitable calibration parameters and accordingly modify the  
 605 reflections at the free top surface by 0.6 while maintaining pure reflections at the solid  
 606 bottom boundary. Figure 9 demonstrates the necessity of accounting for this energy loss.

## 5. Interactions of finite-width internal wave beams

### 5.1. Introduction

The literature on internal wave laboratory experiments can be divided into two broad lines of enquiry: work following from Görtler (1943) and Mowbray & Rarity (1967) on waves generated by a small oscillating body, and work on quasi-monochromatic line sources following McEwan (1971, 1973). The capability of our magic carpet allows us to span the range between these limiting cases, and although previous work using it (Dobra *et al.* 2021) validated new theoretical predictions in the line-source limit, we seek here to demonstrate the generality of these findings by applying them to an intermediate regime. We examine the interactions of finite-width wave beams a few wavelengths across, since recent explorations of such configurations (Smith & Crockett 2014) have uncovered a rich dynamical structure. We have unparalleled access to observe and analyse such wave fields processed first with Synthetic Schlieren and then with Dynamic Mode Decomposition (DMD, Schmid 2010). For the cases we consider here, DMD is an ideal tool because the frequency discretisation is responsive to the input, so it takes many fewer samples to accurately recover the dominant frequencies compared with Fourier methods which project onto basis functions at a fixed discretisation. Furthermore, DMD enables us to distinguish between steady-state behaviours and transient modes. Our experiments have been carefully configured so that steady-state behaviours dominate, and we do not observe the common unsteady phenomenon of triadic resonant instability.

### 5.2. A series expansion for triadic interactions

Building on the recent developments of Dobra *et al.* (2021), here we introduce a fusion of our perturbation expansion framework and the method of solution by Green's function, enabling us to construct general wave fields from the interference patterns produced by a distribution of sources. In Dobra *et al.*, the perturbation expansion at each order yields the internal wave equation in terms of the streamfunction with sources that are Jacobian determinants. Under particular symmetries, we found that these sources cancel, preventing a broad class of wave-wave interactions from occurring. Here, we instead consider configurations where these sources play a significant role in the structure of the wave field, and employing the Green's function with the streamfunction potential, it integrates naturally. We now outline a generalisation of our perturbation framework for these arbitrary wave fields.

We reformulate the conservation of momentum (2.1) and mass (2.3) in terms of streamfunction,  $\psi$ , and buoyancy,  $b = -g\rho'/\rho_{00}$ ,

$$\frac{\partial}{\partial t} \nabla^2 \psi + \left| \frac{\partial(\psi, \nabla^2 \psi)}{\partial(x, z)} \right| = \frac{\partial b}{\partial x}, \quad (5.1a)$$

$$\frac{\partial b}{\partial t} + \left| \frac{\partial(\psi, b)}{\partial(x, z)} \right| = -N^2 \frac{\partial \psi}{\partial x}, \quad (5.1b)$$

where the Jacobian determinant of two scalars,  $\alpha$  and  $\beta$ , is given by

$$\left| \frac{\partial(\alpha, \beta)}{\partial(x, z)} \right| = \frac{\partial \alpha}{\partial x} \frac{\partial \beta}{\partial z} - \frac{\partial \alpha}{\partial z} \frac{\partial \beta}{\partial x}. \quad (5.2)$$

Eliminating the linear  $b$  terms leaves the nonlinear internal wave equation,

$$\frac{\partial^2}{\partial t^2} \nabla^2 \psi + N^2 \frac{\partial^2 \psi}{\partial x^2} = \frac{\partial}{\partial t} \left| \frac{\partial(\nabla^2 \psi, \psi)}{\partial(x, z)} \right| + \frac{\partial}{\partial x} \left| \frac{\partial(b, \psi)}{\partial(x, z)} \right|. \quad (5.3)$$

647 Nonlinearity associated with triadic interactions is captured by source terms of the form  
 648 of Jacobian determinants, and here we consider their behaviour in the case

$$649 \quad \psi = \sum_{j=1}^3 \left\{ A_j \exp \left( i \left[ \mathbf{k}_j \cdot \mathbf{x} - \omega_j t \right] \right) + A_j^* \exp \left( -i \left[ \mathbf{k}_j \cdot \mathbf{x} - \omega_j t \right] \right) \right\}, \quad (5.4)$$

650 where we require complex conjugate (\*) pairs to represent real wave fields. The source  
 651 terms multiply pairs of waves, so we must consider each possible pairing in turn. Self  
 652 interactions equate to zero (McEwan 1973; Tabaei & Akylas 2003; Dobra *et al.* 2021),  
 653 but the interaction of beam  $j = 1$  with beam  $j = 2$  produces terms proportional to  
 654  $\exp(i[(\mathbf{k}_2 + \mathbf{k}_1) \cdot \mathbf{x} - (\omega_2 + \omega_1)t])$  and  $\exp(i[(\mathbf{k}_2 - \mathbf{k}_1) \cdot \mathbf{x} - (\omega_2 - \omega_1)t])$  and their com-  
 655 plex conjugates. Thus, by index manipulation we may define

$$656 \quad \mathbf{k}_3 = \mathbf{k}_2 \pm \mathbf{k}_1, \quad (5.5a)$$

$$657 \quad \omega_3 = \omega_2 \pm \omega_1. \quad (5.5b)$$

659 Should this disturbance characterised by  $\mathbf{k}_3$  and  $\omega_3$  satisfy the dispersion relation (2.7),  
 660  $\omega_3 = Nk_3/|\mathbf{k}_3|$ , the disturbance is also a wave and the source terms are an eigensolution  
 661 of the internal wave equation (2.9). Such combinations are commonly described as resonant  
 662 triads.

663 We examine in figure 10(a) the geometric permutations of wave triad that may be  
 664 constructed for a given  $\mathbf{k}_1$ ,  $\omega_1$  and fixed frequency  $\omega_2$  but where wavevector  $\mathbf{k}_2$  is  
 665 unconstrained. These triangles are compatible with the selection rules derived by Tabaei  
 666 *et al.* (2005) and Jiang & Marcus (2009) that determine into which quadrants, if any, a new  
 667 wave beam may be emitted. These configurations are typical of wave beams a few wavelengths  
 668 across for which the wavenumber spectra are broad. In these cases, the spectrum of the source  
 669 terms is significant across a patch of wavevector space, as shown in figure 10(b). Wavevectors  
 670 that lie on the dashed locus of dispersion-relation-satisfying  $\mathbf{k}_3$  will resonate, and new waves  
 671 will emerge by mode selection; these correspond to cases where the triangle of wavevectors  
 672 can be closed.

673 No polychromatic solutions containing multiple horizontal phase velocities are known for  
 674 the fully nonlinear equation (5.3), so in Dobra *et al.* (2021), we performed a perturbation  
 675 expansion to give a recursive algorithm that we can truncate at finite order to calculate an  
 676 approximate solution. In this earlier work, we expanded  $\psi$  in powers of a small parameter,  $a$ ,  
 677 which we took to be the wave steepness. Instead, here we modify the expansion to be  
 678  $\psi = \sum_{n=1}^{\infty} \psi_n$ , where each subsequent term drops an order of magnitude, and the expansion  
 679 for  $b$  behaves correspondingly. Then, as our earlier work showed, each order satisfies

$$680 \quad \frac{\partial^2}{\partial t^2} \nabla^2 \psi_n + N^2 \frac{\partial^2 \psi_n}{\partial x^2} = \sum_{p=1}^{n-1} \left\{ \frac{\partial}{\partial t} \left| \frac{\partial(\nabla^2 \psi_p, \psi_{n-p})}{\partial(x, z)} \right| + \frac{\partial}{\partial x} \left| \frac{\partial(b_p, \psi_{n-p})}{\partial(x, z)} \right| \right\}. \quad (5.6)$$

681 There is a cascade of information from lower order to higher, but not in reverse, thus the  
 682 expansion is purely inductive. However, at all orders greater than three, there are contributions  
 683 to frequencies that already exist at lower orders. There is an infinite series of such  
 684 contributions to the wave field, some of which manifest as corrections to existing wave beams  
 685 (as we will see later in figure 14) but may also generate waves propagating in new directions.  
 686 We use the polarisation relation of linear internal waves to calculate  $b = N^2 \int \partial \psi / \partial x \, dt$ .

### 687 5.3. Computational method

688 We use a method based on integration across finite elements to predict the steady-state wave  
 689 field due to two crossing internal wave beams, exploiting the symmetry of the complex



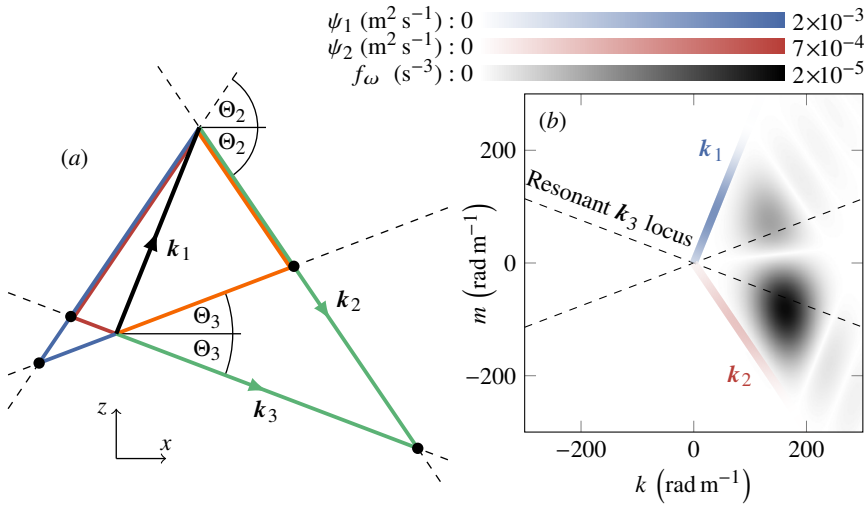


Figure 10: Wavevector triangles for the sum of frequencies  $\omega_1 + \omega_2$  in the case  $\omega_1 = 0.55 \text{ rad s}^{-1} = 0.37N$  and  $\omega_2 = 1.5\omega_1$ . In (a), all permutations of wavevector triangles are presented for the case where  $k_1$  points into the first quadrant. The triangles for all other quadrants are obtained by reflective symmetry. From the dispersion relation (2.7), each frequency has four possible directions for its wavevector, one in each quadrant. Given  $k_1$ , the loci of  $k_2$  and  $k_3$  will in general close to form a triangle in one of four different ways. A closed triangle is a resonant triad. In (b), we plot in greyscale the distribution of source term amplitudes in Fourier space for incident wavevector distributions  $k_1$  (blue) and  $k_2$  (red). The resonant, propagating  $k_3$  lie at the intersections of each of the dashed lines with regions of significant source amplitude. The remainder produce a local interference pattern of forced oscillations. In this configuration, two waves at  $\omega_3$  are emitted: a weaker one with  $k_3$  pointing into the first quadrant (wave propagating down and to the right, triangle marked in orange in (a)), and a stronger one with  $k_3$  pointing into the fourth quadrant (up and to the right, green triangle in (a)).

690 conjugate to avoid unnecessary execution. In the general case, we use a calculation domain  
 691 of  $346 \times 57$  elements with aspect ratio one, and incident waves are produced using an array  
 692 of sources, following the method in §4. For these configurations, we plot  $(1/\rho_{00}) \partial \rho' / \partial z =$   
 693  $(N^2/g) \int (\partial^2 \psi / \partial x \partial z) dt$ .

694 The source terms to the internal wave equation involve third-order derivatives, and any  
 695 errors may propagate across the domain in spurious wave beams. These derivatives are  
 696 recursively applied each time we increase the order of the perturbation expansion. In  
 697 our calculations, we evaluate the expansion to third order and thus the original field is  
 698 differentiated six times. To control numerical noise, we use ghost cells to employ eighth-  
 699 order centred finite differences, and we perform one sweep of elliptic smoothing to eliminate  
 700 mesh-scale truncation error in these derivatives. We take care to ensure that there is a  
 701 separation of length scale between those of the input and those associated with the mesh,  
 702 thus the smoothing has negligible effect on derivatives that contribute to the physics of the  
 703 system.

704 Where we look at the detailed physics of wave-wave interactions, we initialise the  
 705 streamfunction with idealised waveforms corresponding to magic carpet displacement  
 706 profiles,

$$707 \quad h = A \exp(i[kx - \omega t]) \cos^3\left(\frac{\pi}{L}x\right) \text{H}\left(\frac{L}{2} - |x|\right). \quad (5.7)$$

708 The amplitude of the wave,  $A$ , and the width of the envelope,  $L$ , are configured to match  
 709 the experiments, which themselves are configured to approximate the asymptotic limit of a  
 710 wave beam propagating in a viscous fluid (Hurley & Keady 1997; Sutherland *et al.* 1999).  
 711 However, such waveforms have a broad spectrum including both left- and right-travelling  
 712 waves (see Dobra *et al.* 2019). To produce a unidirectional wave, we nullify Fourier modes  
 713 according to their sign and transform back into physical space, a procedure known as the  
 714 Hilbert transform (Mercier *et al.* 2008). Then, we project this profile along the characteristics,  
 715 using cubic spline interpolation to obtain element-centred values. For these calculations, we  
 716 use a grid of  $128 \times 128$  elements with aspect ratio that are non-unity.

#### 717 5.4. Experimental method

718 We use the same experimental apparatus and diagnostics as §4. To maximise the amplitudes of  
 719 the wave beams without inducing locally separated flow near the magic carpet, the amplitudes  
 720 are increased linearly from rest before reaching a steady state. Data acquisition is performed  
 721 over two minutes in this steady state. To build on the work of Tabaei *et al.* (2005), Jiang  
 722 & Marcus (2009) and Smith & Crockett (2014), we seek to examine multiple orientations  
 723 of incident wave beams and achieve these by exploiting reflections off the free surface, as  
 724 shown in figure 11(a).

725 Here, we use the technique of Dynamic Mode Decomposition (DMD, Schmid 2010)  
 726 to identify the temporal modes of a video sequence. Closely related to proper orthogonal  
 727 decomposition, the method takes an observable representation of the system's state,  $\mathbf{y}$ , and  
 728 finds the best-fit system evolution operator,  $\mathbf{A}$ , such that  $d\mathbf{y}/dt = \mathbf{A}\mathbf{y}$  when averaged over  
 729 some period. If  $\mathbf{Y}$  is composed of a temporal sequence of column vectors of states  $\mathbf{y}$  and  
 730 we let  $\mathbf{Y} = \mathbf{U}\mathbf{\Sigma}\mathbf{V}^T$  be its singular value decomposition, then  $\hat{\mathbf{U}}$  may denote a truncation  
 731 of  $\mathbf{U}$  that only includes modes with important singular values. Performing an approximate  
 732 principal axis transformation of  $\mathbf{A}$  to the truncated basis  $\hat{\mathbf{U}}$  and then an eigendecomposition  
 733 of  $\mathbf{A}$  in the new basis, we have

$$734 \quad \mathbf{A} \approx \hat{\mathbf{U}}\hat{\mathbf{A}}\hat{\mathbf{U}}^T = \hat{\mathbf{U}}\hat{\mathbf{W}}\hat{\mathbf{\Lambda}}\hat{\mathbf{W}}^{-1}\hat{\mathbf{U}}^T. \quad (5.8)$$

735 The dynamic modes are the pairing  $\hat{\mathbf{U}}\hat{\mathbf{W}}$ , and generally they each have distinct complex  
 736 conjugate pairs of eigenvalues, whose phases determine their frequencies. They may be  
 737 independently evolved in time, but here we plot these modes evaluated at a common time  
 738 origin.

#### 739 5.5. Results and discussion

740 We begin by comparing our numerical prediction with the output of the Synthetic Schlieren  
 741 in figure 11 using parameters as given in table 2. We highlight each visible wave beam  
 742 schematically in figure 11(c) using the colours blue, red, green and orange to indicate  
 743 successive orders of the perturbation expansion in §5.2. Our priority is to examine wave–  
 744 wave interactions, and while there are many in this figure, the principal interaction zone  
 745 is outlined by the grey box. Since this will be our region of focus for subsequent results,  
 746 we take care to optimise the wave field geometry for diagnostic quality in this region. For  
 747 our prediction to match well, we account for experimental artefacts such as weak viscous  
 748 spreading of wave beams and some unavoidable curvature in the stratification near the top and  
 749 bottom boundaries, so we make small perturbations to waves generated on the synthetic wave  
 750 maker to ensure that waves incident to the boxed region have beam widths and amplitudes  
 751 that match the experiment. Given comprehensive frequency-decomposed post-processing of  
 752 experiments, we are able to perform a thorough calibration of the transmission efficiency  
 753 from order to order. We find by line-search optimisation that it takes a globally constant

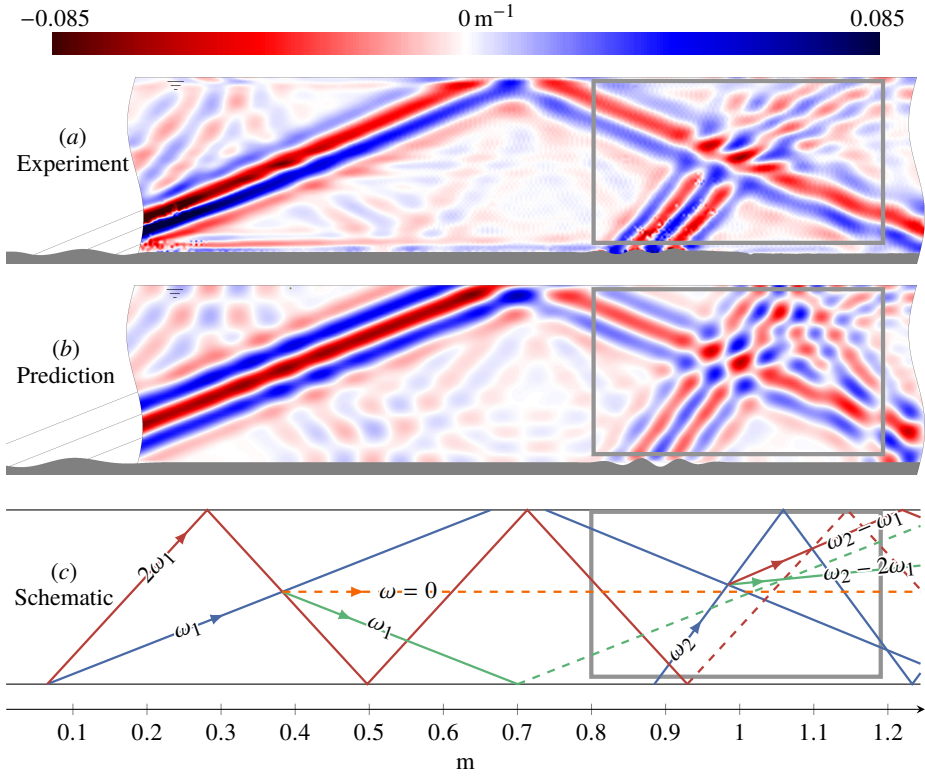


Figure 11: Geometry of wave beams in tank for intersecting two internal waves with the same horizontal direction and opposite vertical direction of the group velocity.

Subfigure (a) shows our experiment, subfigure (b) shows our corresponding prediction, and subfigure (c) shows a schematic of all visible wave beams with blue, red, green and orange corresponding to first-, second-, third- and fourth-order waves respectively.

Beam 1, of frequency  $\omega_1 = 0.55 \text{ rad s}^{-1} \approx 0.37N$ , is generated at the left end of the wave maker, then reflects off the free surface to intersect beam 2, of frequency  $\omega_2 = 2.2\omega_1$ . Among others, a triadic interaction generates a third wave beam at frequency  $\omega_2 - \omega_1$  in the grey rectangle, which is the region of interest in subsequent figures. The diagnostic shown is the vertical gradient of the normalised density perturbation,  $(1/\rho_{00}) \partial \rho' / \partial z$ .

754 value of  $\sim \frac{1}{2}$  across all interactions and all experiments. It remains an open question why  
 755 the perturbation expansion requires such order-to-order calibration, but by matching our  
 756 hierarchical decomposition with suitably post-processed experiments, we have identified a  
 757 discrepancy that could not have been anticipated in advance.

758 In the primary interaction zone, two significant new waves are emitted up and to the right:  
 759 one at second order (shown in red in figure 11(c)) of frequency  $\omega_2 - \omega_1$  due to the interaction  
 760 of beam 2 with beam 1, and the other at third order (shown in green) of frequency  $\omega_2 - 2\omega_1$   
 761 due to the interaction of the first additional wave with beam 2. Where the reflections of both  
 762 beams 1 and 2 intersect, we note an interference pattern leads to a distortion of the phase  
 763 lines in the bottom-right corner of the grey box.

764 The left end of the magic carpet, just outside our diagnostic field of view in the experiment  
 765 (and replicated in the numerical prediction), also emits a second harmonic for beam 1,  
 766 which reflects off the free surface before interacting with its fundamental beam. From this  
 767 interaction, an additional wave of frequency  $\omega_1$  (shown in green in figure 11(c)) is emitted  
 768 though here its direction is down and to the right. This beam reflects off the bottom boundary

Figure	11	12	13	14	15
$N$ (rad s <sup>-1</sup> )	1.50	1.47	1.47	1.41	1.48
$\omega_1$ (rad s <sup>-1</sup> )	0.55	0.55	0.55	0.4	0.8
$k_1$ (rad m <sup>-1</sup> )	39	26	36	48	80
$A_1$ (mm)	2.8	1.8	1.4	1.8	2.6
$L_1$ (m)	0.42	0.34	0.25	0.30	0.12
$\omega_2$ (rad s <sup>-1</sup> )	1.21	1.21	0.825	1.2	1.2
$k_2$ (rad m <sup>-1</sup> )	121	110	75	-40	100
$A_2$ (mm)	1.8	1.7	1.4	4.2	2.4
$L_2$ (m)	0.26	0.18	0.15	0.14	0.11

Table 2: Parameters for each configuration considered, as defined by (5.7).

769 and also happens to intersect the primary interaction zone. Since the second harmonic is  
770 present only at second order (Dobra *et al.* 2021), this additional  $\omega_1$  beam is third-order, so  
771 for a prediction truncated at third order, we do not include any of its interactions with other  
772 wave beams. Also visible in the experiment is a fourth-order zero-frequency wave (shown  
773 in orange) arising from the interaction of the first- and third-order waves of frequency  $\omega_1$ .  
774 While strictly zero-frequency modes cannot propagate, in the asymptotic limit, they closely  
775 resemble gravity currents generated by transient irreversible displacement of mass. Indeed,  
776 these also form near the bottom boundary, and we attribute this small aberration to boundary-  
777 layer mixing.

778 On its third reflection, the second harmonic of  $\omega_1$  intersects its fundamental once more, this  
779 time just after its own reflection off the free surface. We calibrate the strength of reflections  
780 in our predictions to account for surface wave transmission away from reflection sites, and  
781 we find an absorption coefficient of 30%. Furthermore, evaporative cooling acts to smooth  
782 the top interface, which in turn creates complex reflection geometries; we account for these  
783 by applying a phase shift and a higher absorption coefficient of 55% to beam 1 only.

784 In figure 12 for a similar configuration, we expand out all the wave contributions at each  
785 order and frequency, and compare with the DMD of the experiment. We restrict the viewing  
786 window to the grey box in figure 11. The first row contains the superposition of all the wave  
787 beams at each order of truncation. At first order, there are no interactions, so we have only  
788 the linear superposition of incident waves. At second order, we obtain by triadic interactions  
789 a new pair of frequencies,  $\omega_2 - \omega_1$  and  $\omega_2 + \omega_1$ .

790 Eight triads are possible at third order, formed from each combination of a first-order and  
791 a second-order wave, and in each combination both difference and sum of frequencies may  
792 emerge. Four of these triads produce new frequencies, meanwhile there is a pair of triads  
793 from which will emerge new contributions to  $\omega_1$  and a corresponding pair for  $\omega_2$ . The triads  
794 for  $\omega_1$  are  $-(\omega_2 - \omega_1) + \omega_2$  and  $(\omega_2 + \omega_1) - \omega_2$ , and for  $\omega_2$ , they are  $(\omega_2 - \omega_1) + \omega_1$  and  
795  $(\omega_2 + \omega_1) - \omega_1$ . For the configuration in this figure, these contributions are present but very  
796 weak and must not be confused with the third-order  $\omega_1$  wave in the bottom-left that, similarly  
797 to figure 11, arises from the interaction of  $2\omega_1$  and  $\omega_1$  well to the left of the viewing window;  
798 we verified the wave direction in the experiment using the Hilbert transform. We also note  
799 that at third order, there are neither contributions to  $\omega_2 - \omega_1$  nor  $\omega_2 + \omega_1$ ; such additional  
800 contributions only appear from fourth order onwards.

801 Of the new frequencies generated at third order, only  $\omega_2 - 2\omega_1$  has appreciable amplitude.  
802 This propagating wave bends on the boundary of the interaction zone, because dominant

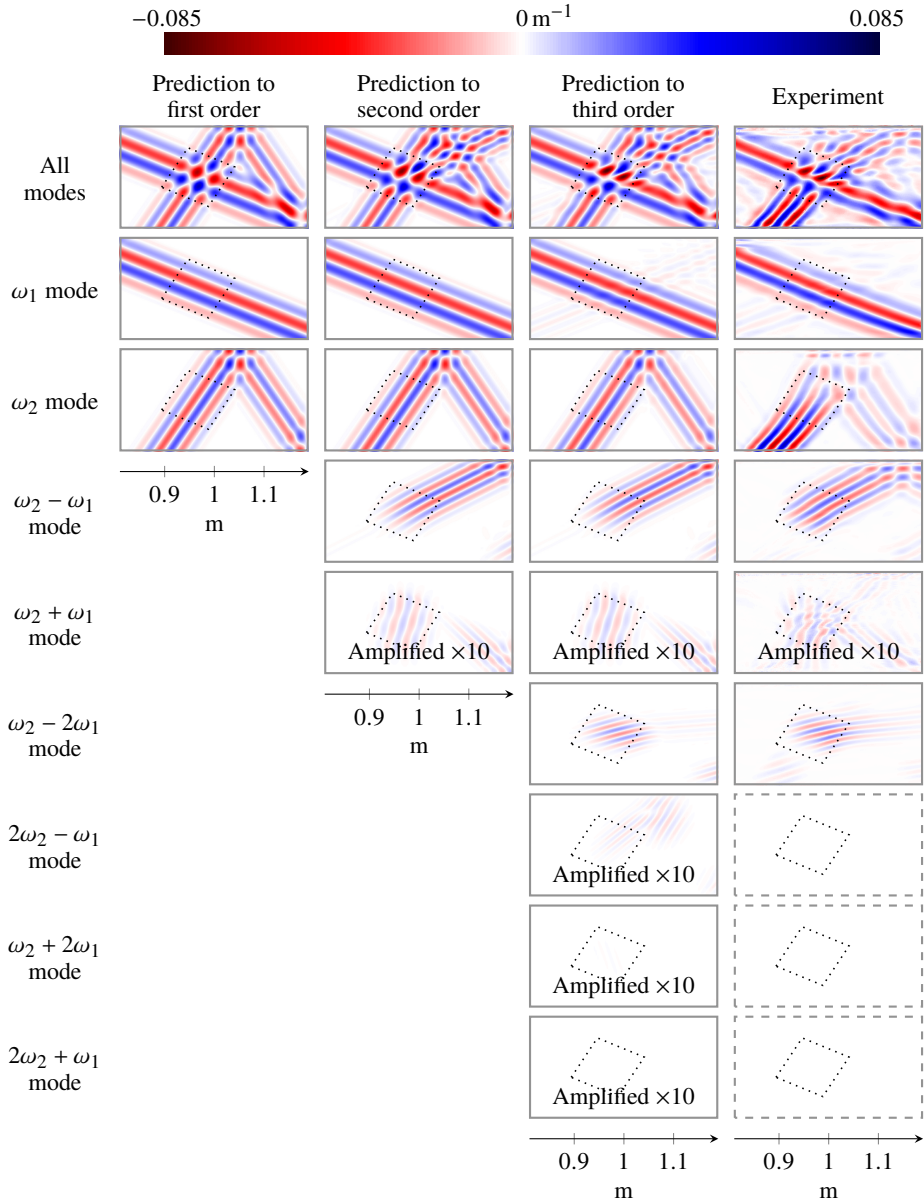


Figure 12: Hierarchical decomposition of the internal wave field where  $\omega_1 \approx 0.37N$  and  $\omega_2 = 2.2\omega_1$ . We plot the real part of evolutionary modes of the diagnostic,  $(1/\rho_{00}) \partial \rho' / \partial z$ , and for reference mark the parallelogram where the incident waves cross with dotted lines. At first order in the expansion, we only obtain the incident waves. At second order, we obtain  $\omega_2 - \omega_1$  and  $\omega_2 + \omega_1$ . At third order, we not only obtain four new frequencies, but we obtain new contributions to  $\omega_1$  and  $\omega_2$  that in this configuration are small in amplitude but broaden the wave beams. There are no further contributions to  $\omega_2 - \omega_1$  and  $\omega_2 + \omega_1$  until fourth order. The final column compares with DMD, and the dashed grey boxes indicate where experimental noise obscured the frequency from detection. We do not constrain the DMD to deliver prescribed frequencies; the best-fit modes are always returned.

803 wavevectors in the source terms do not satisfy the dispersion relation so the associated  
 804 modes are confined as forced oscillations, meanwhile the slightly weaker resonant modes  
 805 are preferentially selected and propagate away from the interaction zone. We also note other  
 806 artefacts visible in both the experiment and the prediction at this frequency. The other three  
 807 new frequencies are evanescent and are too weak to have significant singular values when  
 808 computing the DMD, so we represent these missing modes by boxes with dashed borders.

809 As noted by Bourget *et al.* (2014), the amplitudes of new propagating waves, such as  $\omega_2 -$   
 810  $\omega_1$ , grow linearly across the interaction zone where the source terms are large. Outside this  
 811 zone, propagating over an area with insignificant sources, they have approximately constant  
 812 amplitude. Conversely, forced oscillations have amplitudes that are proportional to the local  
 813 source terms. In this example,  $\omega_2 + \omega_1 > N$  and produces weak evanescent modes that decay  
 814 exponentially with distance from the interaction zone, so we amplify its images by a factor  
 815 of ten. We see a second generation zone of this mode where the reflection of  $\omega_2$  intersects  
 816  $\omega_1$  again in the bottom-right of the domain.

817 Figure 13 is similar to the previous two cases, but configured such that  $\omega_2 + \omega_1 < N$ .  
 818 This mode is emitted to the right both upwards and downwards, but the upwards-propagating  
 819 mode is stronger and noticeably reflects several times within our field of view, thus the  
 820 configuration is dense with opportunities for third-order interactions in the right half of the  
 821 image. One such interaction is the broad addition to  $\omega_2$  in the bottom-right corner, and there  
 822 is a corresponding beam at  $\omega_1$  in the top-right corner.

823 Due to our choice here of  $\omega_2 = 1.5\omega_1$ , some frequencies are duplicated by multiple modes.  
 824 In particular,  $|\omega_2 - 2\omega_1| = \omega_2 - \omega_1$ , but geometrically the wavevectors cannot organise to  
 825 form a contribution from  $\omega_2 - 2\omega_1$ , consistent with the selection rules of Tabaei *et al.*  
 826 (2005) and Jiang & Marcus (2009). In addition, a reflection of the second harmonic of  
 827 beam 1 passes close to the interaction zone, and its interaction with beam 2 near the left  
 828 vertex of the main interaction zone also produces two waves at  $\omega_2 - \omega_1$ , which propagate  
 829 in each of the downward directions. Although the dominant components of  $2\omega_1$  and  $\omega_1$   
 830 have a common horizontal phase velocity and thus have a symmetry that prevents them  
 831 from interacting (Dobra *et al.* 2021), each wave beam is monochromatic in frequency but  
 832 has a broad wavenumber spectrum, so provided we satisfy the geometric selection rules,  
 833 a full spectrum of resonant modes will still be generated. Moreover,  $2\omega_1$  has third-order  
 834 interactions with  $\omega_1$  and  $\omega_2$ , but the only appreciable contribution is  $2\omega_1 + \omega_1 = 3\omega_1$ .  
 835 One component of this signal is a weak evanescent second harmonic of beam 2, visible in  
 836 the bottom-left corner, and appears here because  $2\omega_2 = 3\omega_1$  by construction. However, the  
 837 dominant signal in the DMD mode at  $3\omega_1$  is a forced oscillation associated with beam 2, and  
 838 we do not consider this mechanism in our model, so a direct comparison cannot easily be  
 839 drawn.

840 In numerous places, our experiment demonstrates the presence of yet higher-order  
 841 interactions. Firstly, in the bottom-right corner of the  $\omega_2 - \omega_1$  panel, there is a broadening  
 842 of this wave beam that appears analogous to the previously noted third-order contributions  
 843 to  $\omega_1$  and  $\omega_2$ . This contribution may be generated by a fourth-order interaction between  $\omega_1$   
 844 and the  $\omega_2 - \omega_1$  component that is itself generated by the second harmonic,  $2\omega_1$ , and its  
 845 fundamental,  $\omega_1$ . Secondly, the DMD at  $2\omega_2 - \omega_1$  exhibits waves originating in the main  
 846 interaction zone. We do not predict them at third order, but do expect to find them at higher  
 847 orders. Although our prediction of their amplitudes is poor, we do capture elements of  
 848 their structure. We also note that in the top-right corner, we have successfully predicted the  
 849 third-order interaction  $(\omega_2 - \omega_1) + \omega_2$ .

850 In the following figures, we select some interesting alternative geometries. Figure 14  
 851 considers the interaction of left- and right-running waves, and figure 15 considers incident  
 852 waves from the same quadrant that interact obliquely.

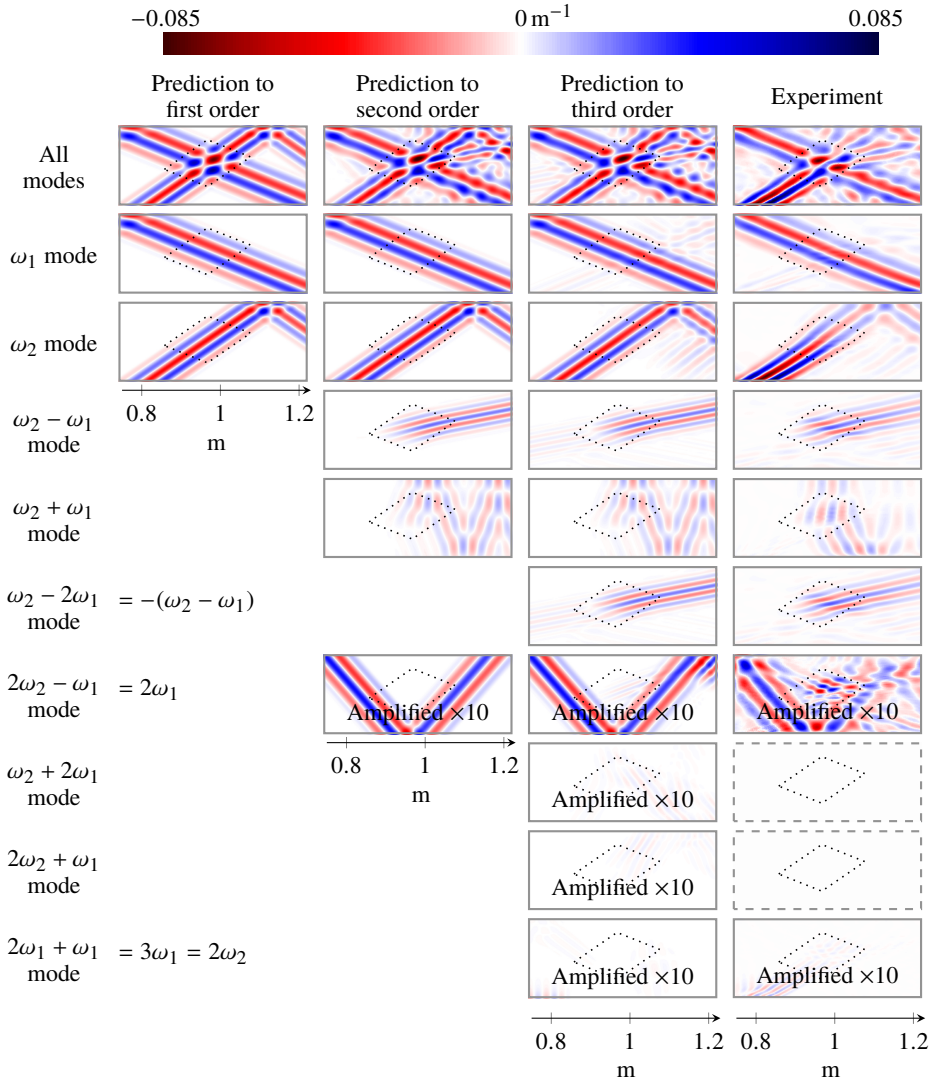


Figure 13: Hierarchical decomposition of the internal wave field where  $\omega_1 \approx 0.37N$  and  $\omega_2 = 1.5\omega_1$ . We plot the real part of evolutionary modes of the diagnostic,  $(1/\rho_{00}) \partial \rho' / \partial z$ , and for reference mark the parallelogram where the incident waves cross with dotted lines. Here,  $\omega_2 + \omega_1 < N$ , so new waves can be emitted. This corresponds to the geometry presented in figure 10, and we see that these waves are emitted in two directions. In this case, several frequencies are duplicated by contributions from multiple sources; in particular,  $|\omega_2 - 2\omega_1| = |\omega_2 - \omega_1|$ . Other duplicates arise from the second harmonic of beam 1, which first appears at second order and just misses the main interaction zone. The final column compares with DMD, and the dashed grey boxes indicate where experimental noise obscured the frequency from detection.

853 With waves in opposite horizontal directions, we have the opportunity to maximise the  
 854 interaction strength by choice of frequencies. The source terms arise from the  $\mathbf{u} \cdot \nabla$  advection  
 855 operators in the governing equations (2.1) and (2.3). The velocity,  $\mathbf{u}$ , points along the wave  
 856 beam, meanwhile all gradients are perpendicular to the beam. In the case where the two beams  
 857 are orthogonal,  $\mathbf{u}$  of one beam is aligned with the gradient vector of the other, and thus the

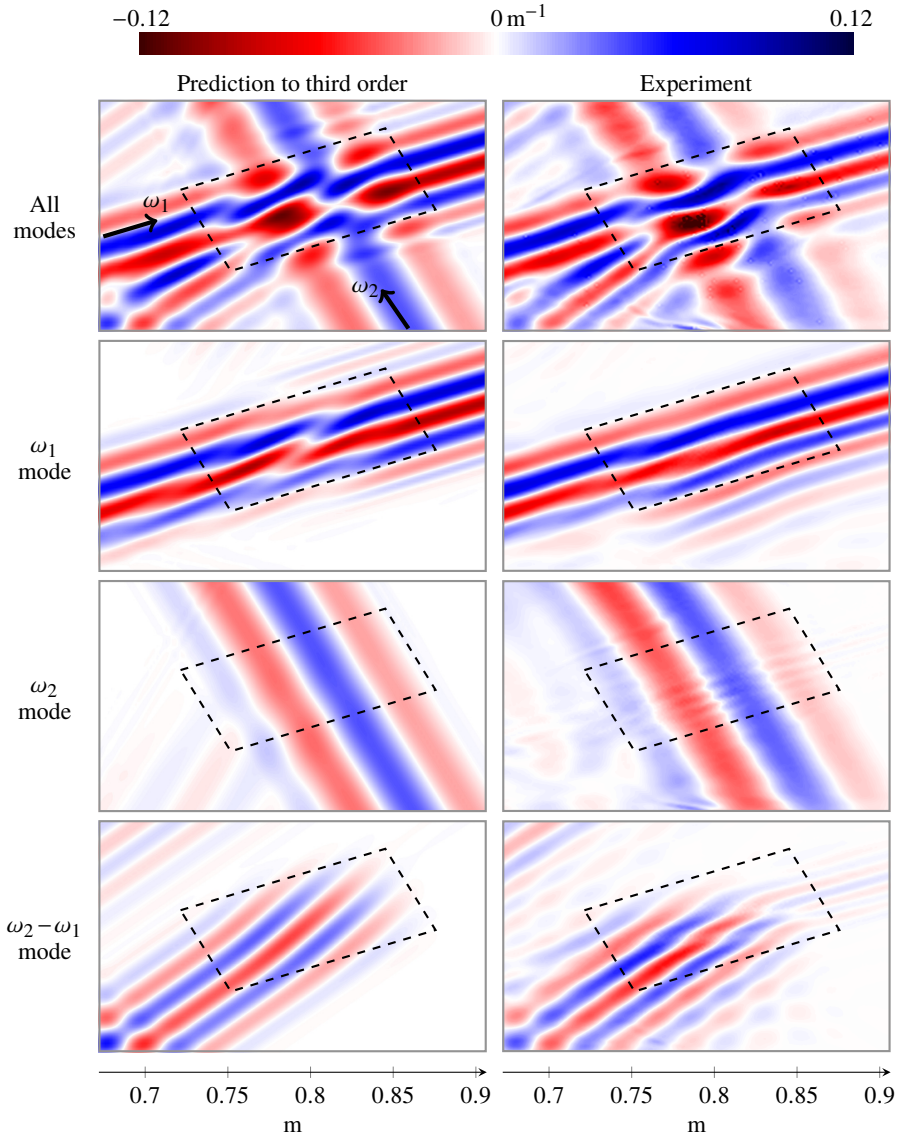


Figure 14: Decomposition of the internal wave field where  $\omega_1 \approx 0.28N$  and  $\omega_2 = 3\omega_1$ . We plot the real part of evolutionary modes of the diagnostic,  $(1/\rho_{00}) \partial \rho' / \partial z$ , and for reference mark the parallelogram where the incident waves cross with dotted lines. We notice in particular distortion of phase lines of  $\omega_1$  due to third-order contributions. For completeness, we include the second harmonic of  $\omega_1$ , since this has the same frequency as  $\omega_2 - \omega_1$ .

858 source terms will be maximal. In figure 14, we demonstrate a near-orthogonal configuration  
 859 with the additional property that the dominant  $\mathbf{k}_2 - \mathbf{k}_1$  is near-resonant.

860 Due to these strong interactions at second order, we have a clear view of the third-order  
 861 contributions to  $\omega_1$ . These broaden the beam significantly, introduce a distortion of the  
 862 phase and slightly increase the amplitude. In addition, the second harmonic of beam 1 has  
 863 frequency  $\omega_2 - \omega_1$  and appears in the top-left corner, which interacts with its fundamental  
 864 beam to produce third-order forced oscillations at  $\omega_1$  whose wavevectors do not align with



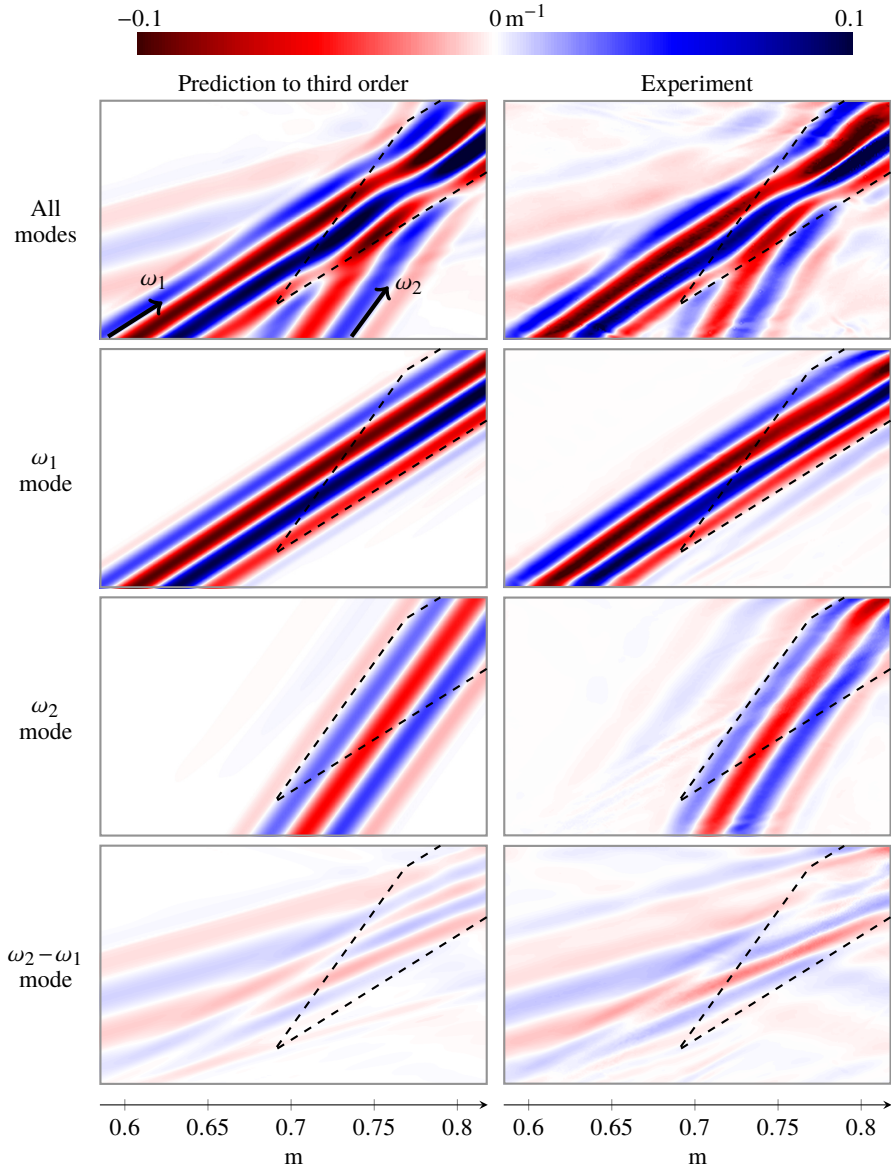


Figure 15: Decomposition of the internal wave field where  $\omega_1 \approx 0.54N$  and  $\omega_2 = 1.5\omega_1$ . We plot the real part of evolutionary modes of the diagnostic,  $(1/\rho_{00}) \partial \rho' / \partial z$ , and for reference mark the parallelogram where the incident waves cross with dotted lines. We observe that beams 1 and 2 exhibit broadening at third order.

865 those of beam 1. Of the remaining contributions to  $\omega_1$ , we distinguish between the following  
 866 permutations: the standard pairings of  $-(\omega_2 - \omega_1) + \omega_2$  and  $(\omega_2 + \omega_1) - \omega_2$ , and an additional  
 867 possible interaction,  $(\omega_2 - \omega_1) - \omega_1$ , whose frequency coincides with  $\omega_1$  in this configuration.  
 868 It turns out that the additional interaction produces a wave that propagates down and to the left,  
 869 whereas the standard pairings produce waves that propagate in the same direction as beam 1  
 870 and are responsible for broadening the beam. Given this clarity, we revisit the  $\omega_1$  and  $\omega_2$  panels  
 871 in figures 12 and 13, and we note that the DMD shows clear distortion of  $\omega_2$ . Although we

872 underpredict the additional  $\omega_2$  contribution, further numerical investigations have confirmed  
 873 that this third-order contribution is primarily responsible for the observed distortion of phase.  
 874 Other less significant factors are due to slight curvature of the stratification, which causes  
 875 waves to refract.

876 Returning to figure 14, at third order in  $\omega_2$ , a weak wave is emitted down and to the left,  
 877 which we have determined from source terms must arise from the interaction  $(\omega_2 - \omega_1) + \omega_1$ .  
 878 Furthermore, the  $\omega_2 - \omega_1$  beam is broader than the main interaction zone in a manner  
 879 analogous to the broadening of  $\omega_1$ , and we attribute this to higher-order contributions.

880 It is of interest that the wavevector of the signal in the top-right of the  $\omega_2 - \omega_1$  experimental  
 881 image is not aligned with the direction given by the dispersion relation, so we conclude that  
 882 these are forced oscillations. Since no other wave beams intersect beam 1 in this region,  
 883 we deduce that these forced oscillations must be driven by the interaction of beam 1 with  
 884 itself, but a single inviscid wave cannot self-interact because its gradients are strictly normal  
 885 to its velocities. If a process, such as viscous spreading of the wave beam, were to cause  
 886 the direction of some wavevectors to vary, triadic interactions would then be possible. We  
 887 consider the sum of two modulated modes. Should the variations in direction be small,  
 888 the wavevectors of the sources must point approximately in the direction of  $2\mathbf{k}_1$ , and thus  
 889 these wavevectors would be narrowly distributed about the resonant locus at the fundamental  
 890 frequency,  $\omega_1$ , represented by a straight line through the origin. These wavevectors would not  
 891 intersect the resonant locus of the second harmonic, which is also a straight line through the  
 892 origin but has steeper gradient, and thus no propagating waves would be emitted at  $2\omega_1$ . We  
 893 hypothesise that such viscous mechanisms are responsible for these features, and in general,  
 894 these are likely to be strongest close to the magic carpet. Indeed, in the  $3\omega_1$  DMD mode of  
 895 figure 13, we notice the same feature and attribute viscous action to its appearance.

896 Figure 15 shows an oblique interaction where the  $\omega_2 - \omega_1$  beam is emitted back into  
 897 the same quadrant from which the incident waves originate. Once again, the interactions  
 898 are strong, and we successfully capture third-order beam-broadening contributions to both  
 899  $\omega_1$  and  $\omega_2$ . Furthermore, we find shifts in phase to the left of the main interaction zone  
 900 at both  $\omega_2$  and  $\omega_2 - \omega_1$ , and a propagating beam down and to the right at  $\omega_2 - \omega_1$ . This  
 901 frequency includes both second- and third-order effects because again  $\omega_2 = 1.5\omega_1$ . In the  
 902 top-left of the DMD mode at this frequency, there is another weak wave that we attribute to  
 903 a higher-order interaction. Finally, we remark that in this experiment, it turned out that there  
 904 was a smooth, weak variation in buoyancy frequency from top to bottom.

## 905 6. Conclusions

906 We have developed a robust hierarchically organised prediction tool for arbitrarily complex  
 907 two-dimensional internal wave systems and contend that this is a necessary and sufficient  
 908 model for determining the structure of wave–wave interactions near the inviscid limit. In this  
 909 work, we introduce for the first time the fusion of a weakly nonlinear perturbation expansion  
 910 with a semi-analytical implementation of the monochromatic free-space Green’s function  
 911 for the governing equation. Our method has indeed been shown to accurately recover the  
 912 structure of wave–wave interactions, showing a remarkable level of agreement between our  
 913 experiments and our method. Having carefully validated our approach using frequency-  
 914 decomposed post-processing, we have now been able to identify wave–wave interactions  
 915 up to third order by direct comparison and infer the origins of other features observed in  
 916 experiments that must arise from higher orders or from secondary effects. This unparalleled  
 917 access to individual components and isolation of interaction behaviour provides clarity to  
 918 the mechanisms in the system, and we have attempted to explain with reference to the weakly  
 919 nonlinear perturbation expansion previously unnoticed physical features, such as forced

920 oscillations that share a frequency with other waves but do not satisfy the dispersion relation  
 921 for a wave to form. Furthermore, we have strong evidence of a previously undiscovered open  
 922 question regarding the order-to-order transmission efficiency of wave–wave interactions.

923 As necessitated by our choice of experimental validation, we have already generalised  
 924 our approach to aperiodic configurations and arbitrary time dependence. With careful  
 925 consideration of causality, we have also provided our calculations for a range of boundary  
 926 conditions for two field potentials so that our free-space source implementation is suitable  
 927 for bounded flows and, in particular, for our case that includes a flexible boundary. We have  
 928 configured our implementation to be minimally elaborate while remaining causal.

929 We remark that there is no particular restriction to systems of internal waves. Our  
 930 hierarchical decomposition is equally valid for any system for which a Green’s function  
 931 may be obtained. These include gravito-inertial systems, Rossby waves and some aspects  
 932 of nonlinear acoustics. Further generalisations we envisage could include solving the linear  
 933 inverse problem to determine suitable source strengths equivalent to a boundary displacement  
 934 computed from data observed at a distance. Our experimental and numerical study has already  
 935 led us to new insights on specific systems, and we anticipate the approach will be adopted  
 936 for a much broader range of problems in the imminent future.

### 937 **Appendix A. Derivation of monochromatic Green’s function**

938 Repurposing the method of Hurley (1972, 1997), we first calculate the Green’s function for  
 939 evanescent oscillations at  $\omega > N$ , then analytically continue it to other values of  $\omega$ . Defining  
 940 the transformed coordinates to perform a dilatation,

$$941 \quad \begin{bmatrix} x \\ z \end{bmatrix} \mapsto \begin{bmatrix} x_\alpha \\ z_\alpha \end{bmatrix} = \begin{bmatrix} \frac{x}{\Gamma} \\ z \end{bmatrix}, \quad (\text{A } 1)$$

942 the point-forced internal wave equation (3.3) becomes Poisson’s equation in the new  
 943 coordinate system for  $\omega > N$ ,

$$944 \quad \frac{\partial^2 G_\omega}{\partial x_\alpha^2} + \frac{\partial^2 G_\omega}{\partial z_\alpha^2} = -\frac{\delta(x_\alpha - \frac{x_0}{\Gamma}) \delta(z_\alpha - z_0)}{\Gamma \omega^2}. \quad (\text{A } 2)$$

945 Thus,  $G_\omega$  is proportional to the corresponding free-space Green’s function,

$$946 \quad G_\omega = C - \frac{\log(r^2)}{4\pi\omega^2\Gamma}, \quad (\text{A } 3)$$

947 where  $r^2 = (x - x_0)^2/(1 - (N/\omega)^2) + (z - z_0)^2$  and  $C$  is the integration constant, which is  
 948 a gauge freedom that we take to be zero.

949 We now extend  $G_\omega$  to be valid at all frequencies using analytic continuation in complex  
 950  $\omega$  space. The logarithm has branch points at  $r^2 = \{0, \infty\}$ , which rearranges to

$$951 \quad 1 - \left(\frac{N}{\omega}\right)^2 = \left\{ -\left(\frac{x - x_0}{z - z_0}\right)^2, 0 \right\}, \quad (\text{A } 4)$$

952 and thus the logarithm has four branch points,

$$953 \quad \omega = \left\{ \pm \frac{N}{\sqrt{1 + \left(\frac{x - x_0}{z - z_0}\right)^2}}, \pm N \right\}. \quad (\text{A } 5)$$

954 In addition,  $1/\Gamma$  has three branch points,  $\omega = \{0, \pm N\}$ , so, in total, there are five distinct

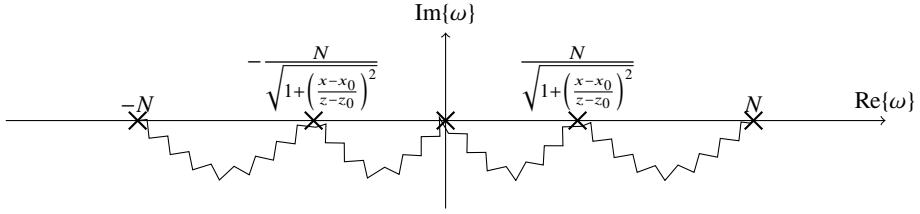


Figure 16: Branch points, shown with crosses, and branch cuts, shown with wiggly lines, for analytic continuation in  $\omega$ . The five branch points are all on the real axis and the branch cut must be in the lower half plane to satisfy causality.

955 branch points, as marked in figure 16. Those at  $\omega = \pm N$  correspond to the regime change  
 956 from evanescent to propagating internal waves. The branch points all need joining with branch  
 957 cuts, which we chose carefully to provide physically realisable conditions. Since any steady-  
 958 state internal wave must have grown from a stationary ambient at some time in the past,  
 959 we assume that the wave is in fact growing exponentially slowly in time and so  $\text{Im}\{\omega\} > 0$   
 960 (Lighthill 1960). Thus, we deform all the branch cuts to below the real line; these are shown  
 961 by the wiggly lines in the figure.

962 To perform the analytic continuation, we consider the complex arguments of the square  
 963 root in  $\Gamma$  and of the logarithm. For complex  $\omega = \omega_r + i\epsilon$  with real part  $\omega_r$  and a small  
 964 imaginary part  $\epsilon$ , we make the expansion

$$965 \quad \frac{1}{\Gamma^2} = \frac{1}{1 - \left(\frac{N}{\omega_r + i\epsilon}\right)^2} = \frac{\omega_r^2(\omega_r^2 - N^2) + (2\omega_r^2 + N^2)\epsilon^2 + \epsilon^4 - 2iN^2\omega_r\epsilon}{(\omega_r^2 - N^2 - \epsilon^2)^2 + 4\omega_r^2\epsilon^2}. \quad (\text{A } 6)$$

966 The denominator is always positive and  $\epsilon \geq 0$ , so  $\text{sgn}(\text{Im}\{1/\Gamma^2\}) = -\text{sgn}(\text{Re}\{\omega\})$ .

967 When  $\omega > N$  and is real, the complex argument,  $\arg(r^2) = 0$ . On proceeding around the  
 968 first branch point at  $\omega = N$ , where  $r^2$  becomes infinite,  $\text{Im}\{1/\Gamma^2\} < 0$ , so  $\text{Im}\{r^2\} < 0$ . Thus,  
 969  $\arg(r^2)$  decreases to become  $-\pi$  for  $N(1 + ((x - x_0)/(z - z_0))^2)^{-1/2} < \omega < N$ ; in other  
 970 words,  $r^2$  increases from  $-\infty$  to zero between these branch points. As  $\omega$  decreases further,  
 971 the term  $(x - x_0)^2/(1 - (N/\omega)^2)$  becomes less significant, such that  $r^2$  becomes positive real  
 972 again after the next branch point,  $N(1 + ((x - x_0)/(z - z_0))^2)^{-1/2}$ , with its argument yet to  
 973 be determined. Since  $\text{Re}\{\omega\} > 0$ , we have  $\text{Im}\{1/\Gamma^2\} < 0$  and hence  $\text{Im}\{r^2\} < 0$ , so  $\arg(r^2)$   
 974 increases around the branch point to become zero for  $-N(1 + ((x - x_0)/(z - z_0))^2)^{-1/2} <$   
 975  $\omega < N(1 + ((x - x_0)/(z - z_0))^2)^{-1/2}$ . The frequency,  $\omega$ , is now negative for the remaining  
 976 two branch points of the logarithm, so the analytic continuation is in the upper half  $\omega$  plane.  
 977 Therefore,  $\arg(r^2) = +\pi$  for  $-N < \omega < -N(1 + ((x - x_0)/(z - z_0))^2)^{-1/2}$  and zero for  
 978  $\omega < -N$ . Thus,  $\text{Re}\{r^2\}$  exhibits even symmetry about  $\omega = 0$  but  $\arg(r^2)$  has odd symmetry.  
 979 The value of the logarithm can now be determined using the standard formula,

$$980 \quad \log(r^2) = \log|r^2| + i \arg(r^2). \quad (\text{A } 7)$$

981 Next, we consider the three branch points of  $1/\Gamma$ . For  $\omega > N$ , its complex argument is  
 982 zero. Proceeding round the first branch point, at  $\omega = N$ ,  $\arg(1/\Gamma^2)$  decreases to  $-\pi$ , so  
 983  $\arg(1/\Gamma) = -\pi/2$  and  $1/\Gamma = -i((N/\omega)^2 - 1)^{-1/2}$  for  $0 < \omega < N$ . The second branch  
 984 point is at  $\omega = 0$ . When  $\epsilon > 0$ ,  $\text{Im}\{1/\Gamma^2\} = 0$  only when  $\text{Re}\{\omega\} = 0$ . At this point,  
 985  $\text{Re}\{1/\Gamma^2\} = \epsilon^2/(N^2 + \epsilon^2) > 0$ , despite being negative when  $\omega$  is significantly away from  
 986 zero. Thus, the analytic continuation path in complex  $1/\Gamma^2$  space goes anticlockwise around  
 987 the branch point, as shown in figure 17. So,  $\arg(1/\Gamma^2) = +\pi$  for  $-N < \omega < 0$ , thus  $1/\Gamma$

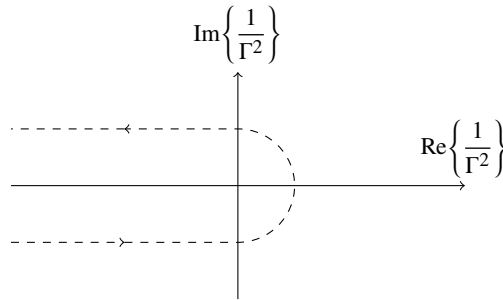


Figure 17: Analytic continuation path of  $1/\Gamma^2$  for decreasing  $\omega$  around 0. In order to satisfy causality,  $\text{Im}\{\omega\} \geq 0$ , so the path shown is obtained by deforming  $\omega$  into the upper half plane. The quantity  $1/\Gamma^2$  is real and negative around  $\omega = 0$ , but the argument of  $1/\Gamma$  changes from  $-\pi$  to  $+\pi$ .

988 changes sign at  $\omega = 0$ . At the final branch point,  $\omega = -N$ ,  $\text{Im}\{1/\Gamma^2\} > 0$ , so its argument  
 989 decreases from  $+\pi$  to zero.

990 The assembled Green's function for each case is listed in table 3.

#### REFERENCES

- 991 BALMFORTH, NEIL J. & PEACOCK, THOMAS 2009 Tidal Conversion by Supercritical Topography. *J. Phys.*  
 992 *Oceanogr.* **39** (8), 1965–1974.
- 993 BENIELLI, DOMINIQUE & SOMMERIA, JOËL 1998 Excitation and breaking of internal gravity waves by  
 994 parametric instability. *J. Fluid Mech.* **374**, 117–144.
- 995 BOURGET, BAPTISTE, DAUXOIS, THIERRY, JOUBAUD, SYLVAIN & ODIER, PHILIPPE 2013 Experimental study of  
 996 parametric subharmonic instability for internal plane waves. *J. Fluid Mech.* **723**, 1–20.
- 997 BOURGET, BAPTISTE, SCOLAN, HÉLÈNE, DAUXOIS, THIERRY, LE BARS, MICHAEL, ODIER, PHILIPPE & JOUBAUD,  
 998 SYLVAIN 2014 Finite-size effects in parametric subharmonic instability. *J. Fluid Mech.* **759**, 739–750.
- 999 DALZIEL, STUART B., HUGHES, GRAHAM O. & SUTHERLAND, BRUCE R. 1998 Synthetic schlieren. In *Proc.*  
 1000 *8th Int. Symp. Flow Vis.* (ed. Carlomagno & Grant). Paper 062.
- 1001 DALZIEL, S B, HUGHES, G O & SUTHERLAND, B R 2000 Whole-field density measurements by ‘synthetic  
 1002 schlieren’. *Exp. Fluids* **28** (4), 322–335.
- 1003 DALZIEL, STUART B., PATTERSON, MICHAEL D., CAULFIELD, C. P. & LE BRUN, STÉPHANE 2011 The structure  
 1004 of low-Froude-number lee waves over an isolated obstacle. *J. Fluid Mech.* **689**, 3–31.
- 1005 DALZIEL RESEARCH PARTNERS 2018 DigiFlow vv3.6.0–4.2.0. <http://www.dalzielresearch.com/digiflow/>.
- 1007 DAUXOIS, THIERRY, JOUBAUD, SYLVAIN, ODIER, PHILIPPE & VENAILLE, ANTOINE 2018 Instabilities of Internal  
 1008 Gravity Wave Beams. *Annu. Rev. Fluid Mech.* **50**, 131–156.
- 1009 DAVIS, RUSS E. & ACRIVOS, ANDREAS 1967 The stability of oscillatory internal waves. *J. Fluid Mech.* **30** (4),  
 1010 723–736.
- 1011 DOBRA, THOMAS EDWARD 2018 Nonlinear Interactions of Internal Gravity Waves. PhD thesis, University of  
 1012 Bristol.
- 1013 DOBRA, THOMAS E., LAWRIE, ANDREW G. W. & DALZIEL, STUART B. 2019 The magic carpet: an arbitrary  
 1014 spectrum wave maker for internal waves. *Exp. Fluids* **60** (11), 172.
- 1015 DOBRA, THOMAS E., LAWRIE, ANDREW G. W. & DALZIEL, STUART B. 2021 Harmonics from a magic carpet.  
 1016 *J. Fluid Mech.* **911**, A29.
- 1017 FORTUIN, J. M. H. 1960 Theory and application of two supplementary methods of constructing density  
 1018 gradient columns. *J. Polym. Sci.* **44**, 505–515.
- 1019 GÖRTLER, H. 1943 Über eine Schwingungserscheinung in Flüssigkeiten mit stabiler Dichteschichtung.  
 1020 *ZAMM - Zeitschrift für Angew. Math. und Mech.* **23** (2), 65–71.
- 1021 GOSTIAUX, LOUIS, DIDELLE, HENRI, MERCIER, STEPHANE & DAUXOIS, THIERRY 2007 A novel internal waves  
 1022 generator. *Exp. Fluids* **42** (1), 123–130.

Range of $\omega$	Argument of $r^2 \frac{1}{\Gamma}$		Green's function
$\omega > N$	0	0	$-\frac{\log\left(\frac{(x-x_0)^2}{1-\left(\frac{N}{\omega}\right)^2} + (z-z_0)^2\right)}{4\pi\omega^2\sqrt{1-\left(\frac{N}{\omega}\right)^2}}$
$\frac{N}{\sqrt{1+\left(\frac{x-x_0}{z-z_0}\right)^2}} < \omega < N$	$-\pi$	$-\frac{\pi}{2}$	$i\frac{\left\{\log\left(\frac{(x-x_0)^2}{\left(\frac{N}{\omega}\right)^2-1} - (z-z_0)^2\right) - i\pi\right\}}{4\pi\omega^2\sqrt{\left(\frac{N}{\omega}\right)^2-1}}$
$0 < \omega < \frac{N}{\sqrt{1+\left(\frac{x-x_0}{z-z_0}\right)^2}}$	0	$-\frac{\pi}{2}$	$i\frac{\log\left(-\frac{(x-x_0)^2}{\left(\frac{N}{\omega}\right)^2-1} + (z-z_0)^2\right)}{4\pi\omega^2\sqrt{\left(\frac{N}{\omega}\right)^2-1}}$
$-\frac{N}{\sqrt{1+\left(\frac{x-x_0}{z-z_0}\right)^2}} < \omega < 0$	0	$+\frac{\pi}{2}$	$-i\frac{\log\left(-\frac{(x-x_0)^2}{\left(\frac{N}{\omega}\right)^2-1} + (z-z_0)^2\right)}{4\pi\omega^2\sqrt{\left(\frac{N}{\omega}\right)^2-1}}$
$-N < \omega < -\frac{N}{\sqrt{1+\left(\frac{x-x_0}{z-z_0}\right)^2}}$	$+\pi$	$+\frac{\pi}{2}$	$-i\frac{\left\{\log\left(\frac{(x-x_0)^2}{\left(\frac{N}{\omega}\right)^2-1} - (z-z_0)^2\right) + i\pi\right\}}{4\pi\omega^2\sqrt{\left(\frac{N}{\omega}\right)^2-1}}$
$\omega < -N$	0	0	$-\frac{\log\left(\frac{(x-x_0)^2}{1-\left(\frac{N}{\omega}\right)^2} + (z-z_0)^2\right)}{4\pi\omega^2\sqrt{1-\left(\frac{N}{\omega}\right)^2}}$

Table 3: Monochromatic Green's function, including results of analytic continuation, for all cases of  $\omega$ . An integration constant can be added onto the Green's function, but this does not affect derived quantities such as the velocity, so without loss of generality we take it to be zero.

1023 VAN HAREN, HANS, MAAS, LEO & VAN AKEN, HENDRIK 2002 On the nature of internal wave spectra near a  
 1024 continental slope. *Geophys. Res. Lett.* **29** (12), 57.  
 1025 HURLEY, D. G. 1969 The emission of internal waves by vibrating cylinders. *J. Fluid Mech.* **36** (4), 657–672.  
 1026 HURLEY, D. G. 1972 A general method for solving steady-state internal gravity wave problems. *J. Fluid*  
 1027 *Mech.* **56** (4), 721–740.  
 1028 HURLEY, D. G. 1997 The generation of internal waves by vibrating elliptic cylinders. Part 1. Inviscid solution.  
 1029 *J. Fluid Mech.* **351**, 105–118.  
 1030 HURLEY, D. G. & KEADY, G. 1997 The generation of internal waves by vibrating elliptic cylinders. Part 2.  
 1031 Approximate viscous solution. *J. Fluid Mech.* **351**, 119–138.  
 1032 JAVAM, A., IMBERGER, J. & ARMPFIELD, S. W. 2000 Numerical study of internal wave–ÅŞwave interactions  
 1033 in a stratified fluid. *J. Fluid Mech.* **415**, 65–87.  
 1034 JIANG, CHUNG-HSIANG & MARCUS, PHILIP S. 2009 Selection Rules for the Nonlinear Interaction of Internal  
 1035 Gravity Waves. *Phys. Rev. Lett.* **102**, 124502.  
 1036 KARIMI, HUSSAIN H & AKYLAS, T R 2014 Parametric subharmonic instability of internal waves: locally  
 1037 confined beams versus monochromatic wavetrains. *J. Fluid Mech* **757**, 381–402.

- 1038 KOUDELLA, C. R. & STAQUET, CHANTAL 2006 Instability mechanisms of a two-dimensional progressive  
1039 internal gravity wave. *J. Fluid Mech.* **548**, 165–196.
- 1040 LIGHTHILL, M. J. 1960 Studies on Magneto-Hydrodynamic Waves and other Anisotropic Wave Motions.  
1041 *Philos. Trans. R. Soc. A Math. Phys. Eng. Sci.* **252** (1014), 397–430.
- 1042 LIGHTHILL, M. J. 1978 *Waves in Fluids*. Cambridge University Press.
- 1043 MARTIN, S., SIMMONS, W. F. & WUNSCH, C. I. 1969 Resonant Internal Wave Interactions. *Nature* **224** (5223),  
1044 1014–1016.
- 1045 McCOMAS, C. HENRY & BRETHERTON, FRANCIS P. 1977 Resonant interaction of oceanic internal waves. *J.*  
1046 *Geophys. Res.* **82** (9), 1397–1412.
- 1047 McEWAN, A. D. 1971 Degeneration of resonantly-excited standing internal gravity waves. *J. Fluid Mech.*  
1048 **50** (3), 431–448.
- 1049 McEWAN, A. D. 1973 Interactions between internal gravity waves and their traumatic effect on a continuous  
1050 stratification. *Boundary-Layer Meteorol.* **5** (1-2), 159–175.
- 1051 McEWAN, A. D. & ROBINSON, R. M. 1975 Parametric instability of internal gravity waves. *J. Fluid Mech.*  
1052 **67** (4), 667–687.
- 1053 MERCIER, MATTHIEU J., GARNIER, NICOLAS B. & DAUXOIS, THIERRY 2008 Reflection and diffraction of  
1054 internal waves analyzed with the Hilbert transform. *Phys. Fluids* **20**, 086601.
- 1055 MERCIER, MATTHIEU J., MARTINAND, DENIS, MATHUR, MANIKANDAN, GOSTIAUX, LOUIS, PEACOCK, THOMAS  
1056 & DAUXOIS, THIERRY 2010 New wave generation. *J. Fluid Mech.* **657**, 308–334.
- 1057 MOWBRAY, D. E. & RARITY, B. S. H. 1967 A theoretical and experimental investigation of the phase  
1058 configuration of internal waves of small amplitude in a density stratified liquid. *J. Fluid Mech.* **28** (1),  
1059 1–16.
- 1060 MÜLLER, PETER, HOLLOWAY, GREG, HENYEV, FRANK & POMPHREY, NEIL 1986 Nonlinear interactions among  
1061 internal gravity waves. *Rev. Geophys.* **24** (3), 493–536.
- 1062 OSTER, GERALD 1965 Density Gradients. *Sci. Am.* **213** (2), 70–76.
- 1063 PÉTRÉLIS, FRANÇOIS, SMITH, STEFAN LLEWELLYN & YOUNG, W. R. 2006 Tidal Conversion at a Submarine  
1064 Ridge. *J. Phys. Oceanogr.* **36** (6), 1053–1071.
- 1065 PHILLIPS, O. M. 1960 On the dynamics of unsteady gravity waves of finite amplitude. *J. Fluid Mech.* **9** (2),  
1066 193–217.
- 1067 RATTRAY, MAURICE 1960 On the Coastal Generation of Internal Tides. *Tellus* **12** (1), 54–62.
- 1068 ROBINSON, R. M. 1969 The effects of a vertical barrier on internal waves. *Deep Sea Res. Oceanogr. Abstr.*  
1069 **16** (5), 421–429.
- 1070 SCASE, M. M. & DALZIEL, S. B. 2004 Internal wave fields and drag generated by a translating body in a  
1071 stratified fluid. *J. Fluid Mech.* **498**, 289–313.
- 1072 SCHMID, PETER J. 2010 Dynamic mode decomposition of numerical and experimental data. *J. Fluid Mech.*  
1073 **656**, 5–28.
- 1074 SEKERZH-ZEN'KOVICH, S. IA. 1981 Construction of the fundamental solution for the operator of internal  
1075 waves. *J. Appl. Math. Mech.* **45** (2), 192–198.
- 1076 SMITH, S. & CROCKETT, J. 2014 Experiments on nonlinear harmonic wave generation from colliding internal  
1077 wave beams. *Exp. Therm. Fluid Sci.* **54**, 93–101.
- 1078 SUN, HAILI & KUNZE, ERIC 1999a Internal Wave–Wave Interactions. Part I: The Role of Internal Wave  
1079 Vertical Divergence. *J. Phys. Oceanogr.* **29** (11), 2886–2904.
- 1080 SUN, HAILI & KUNZE, ERIC 1999b Internal Wave–Wave Interactions. Part II: Spectral Energy Transfer  
1081 and Turbulence Production. *J. Phys. Oceanogr.* **29** (11), 2905–2919.
- 1082 SUSANTO, R. DWI, MITNIK, LEONID & ZHENG, QUANAN 2005 Ocean internal waves observed in the Lombok  
1083 Strait. *Oceanography* **18** (4), 80–87.
- 1084 SUTHERLAND, B. R., DALZIEL, S. B., HUGHES, G. O. & LINDEN, P. F. 1999 Visualization and measurement  
1085 of internal waves by 'synthetic schlieren'. Part 1. Vertically oscillating cylinder. *J. Fluid Mech.* **390**,  
1086 93–126.
- 1087 SVEEN, J. K. & DALZIEL, S. B. 2005 A dynamic masking technique for combined measurements of PIV and  
1088 synthetic schlieren applied to internal gravity waves. *Meas. Sci. Technol.* **16** (10), 1954–1960.
- 1089 TABAEI, ALI & AKYLAS, T. R. 2003 Nonlinear internal gravity wave beams. *J. Fluid Mech.* **482**, 141–161.
- 1090 TABAEI, ALI, AKYLAS, T. R. & LAMB, KEVIN G. 2005 Nonlinear effects in reflecting and colliding internal  
1091 wave beams. *J. Fluid Mech.* **526**, 217–243.
- 1092 THORPE, S. A. 1966 On wave interactions in a stratified fluid. *J. Fluid Mech.* **24**, 737–751.

- 1093 VOISIN, BRUNO 1991 Internal wave generation in uniformly stratified fluids. Part 1. Green's function and  
1094 point sources. *J. Fluid Mech.* **231**, 439–480.
- 1095 VOISIN, BRUNO 1994 Internal wave generation in uniformly stratified fluids. Part 2. Moving point sources.  
1096 *J. Fluid Mech.* **261**, 333–374.